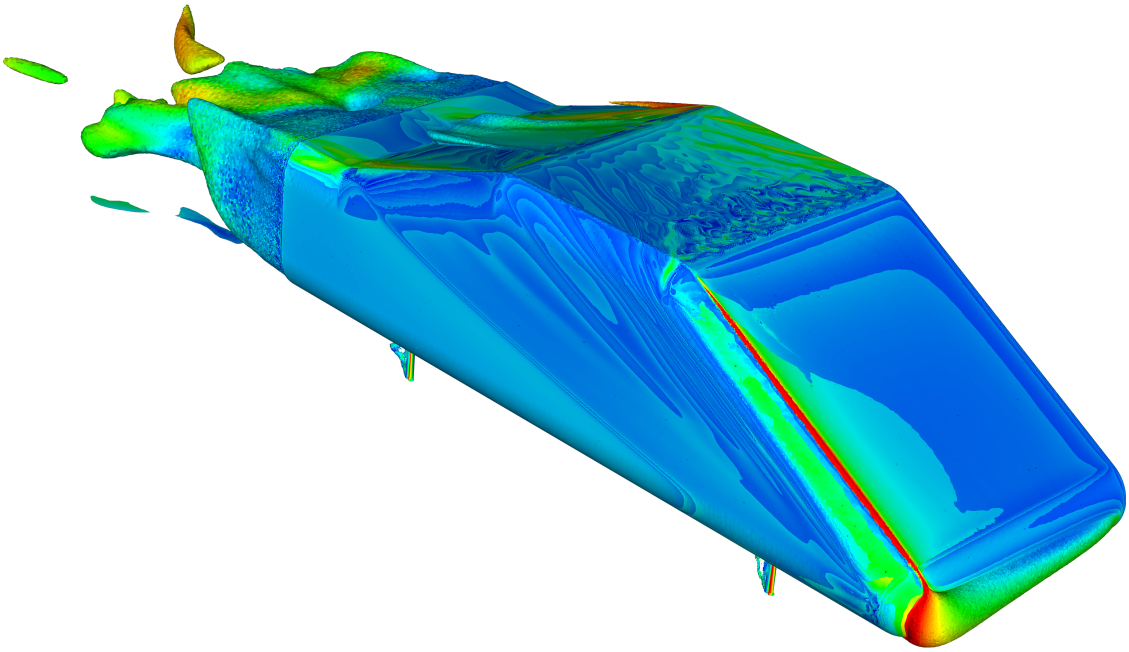

PANS prediction of passenger vehicle flows

Accurate flow prediction for an SAE 20 degree notchback reference body

Master's thesis in Applied Mechanics

Johannes Törnell

Department of Applied Mechanics
CHALMERS UNIVERSITY OF TECHNOLOGY
Gothenburg, Sweden 2016

Master's thesis 2016:85

PANS prediction of passenger vehicle flows

Accurate flow prediction for an SAE 20 degree notchback reference body

Johannes Törnell

CHALMERS
UNIVERSITY OF TECHNOLOGY

Department of Applied Mechanics
Division of Fluid Dynamics
Vehicle Aerodynamic Laboratory
Chalmers University of Technology
Gothenburg, Sweden 2016

PANS prediction of passenger vehicle flows
Accurate flow prediction for an SAE 20 degree notchback reference body
Johannes Törnell

Supervisor: Sinisa Krajnovic, Applied Mechanics
Supervisor: Branislav Basara, AVL
Examiner: Sinisa Krajnovic, Applied Mechanics

Master's Thesis 2016:85
Department of Applied Mechanics
Division of Fluid Mechanics
Vehicle Aerodynamic Laboratory
Chalmers University of Technology
SE-412 96 Gothenburg
Telephone +46 702 79 77 76

Cover: SAE reference body with Q-criterion of instantaneous velocity colored by instantaneous velocity.

Typeset in LaTeX
Printed by [Name of printing company]
Gothenburg, Sweden 2016

PANS prediction of passanger vehicle flows
Accurate flow prediction for an SAE 20 degree notchback reference body and closed cooling XC60
Johannes Törnell
Department of Applied Mechanics
Chalmers University of Technology

Abstract

This thesis was performed at Chalmers University of Technology in cooperation with AVL. The Partially Averaged Navier-Stokes model that was investigated here has the opportunity of being a very powerful tool with promises of being accurate and relatively low cost. In this thesis the PANS model is evaluated for the flow over an SAE 30 degree notchback reference body which is a simplified representation of a car. Two different discretization schemes have been used here and compared to data from tests done on the same model in a wind tunnel. The results show a fairly good agreement with respect to the flow structures and the SMART simulation shows very good agreement with respect to drag and base pressure. The SMART simulation shows many more resolved small flow structures than the MINMOD simulation but also shows separation at a too early point. These results can be summarized as that the model has good potential and is good at predicting flow structures and drag; there is however still a significant amount of work to be done with choosing discretization and investigating the mesh resolution impact on a case like this. Further work on more complex shapes also has to be done however that was not possible in this thesis due to the very difficult meshing in AVL Fire.

Acknowledgements

I would like to thank D Wood et al for creating a good database of experimental data to compare my simulations to and sharing them freely. i would also like to thank Guglielmo Minelli for his help with AVL Fire and guidance in setting up cases. I would also like to thank Anirudh Rao for his help with analyzing some of the data. An areciation should be paid to Branislav Basara at AVL for his help with settings for cases in AVL Fire and providing the thesis. I would also like to thank Jan Viher at AVL for help with meshing and geometry cleanup. Finally I would like to thank my examiner and supervisor Sinisa Krajnovic for the guidance and help during the entire project. I would also like to thank NSC for providing the cluster computing time enabling this project.

Johannes Törnell, Gothenburg, December 2016

Contents

List of Figures

Nomenclature

α^-	Control factor SMART for upstream face
$\bar{\phi}_C$	Normalized Current Cell value
$\bar{\phi}_f$	Normalized Face value
$\bar{\phi}_{i-1/2}$	Normalized face value
$\bar{\phi}_{i-1}$	Normalized Upstream node Value
$\bar{\phi}$	Normalized Cell value
Δ	Geometric average grid cell dimension
$\dot{m}$	Mass flow
Λ	Integral length scale
$\mathcal{P}$	Partial averaging operator
μ	Dynamic viscosity
ν	Kinematic Viscosity
ν_u	Eddy Viscosity
ϕ	Cell value
ϕ_D	Downstream Cell value
ϕ_P	Current Cell value
ϕ_U	Upstream Cell value
ϕ_W	West Cell value
ϕ_w	West face value
ρ	Density
τ_w	Wall shear stress
τ_{ij}	Second order moment
ε	Dissipation
ε_k	Resolved to unresolved dissipation
ε_u	Unresolved Dissipation
φ_f^*	Normalized limiter argument
φ_f	Limiter argument
C_p	Coefficient of Pressure
CD	Central differencing
CFD	Computational Fluid Dynamics
CFL	Courant-Freidichs-Lewy
f_f^*	Flow oriented interpolation factor
f_f	Interpolation factor
f_i	Body Force
f_k	Resolved to unresolved kinetic energy
k	Turbulent kinetic energy
k_u	Unresolved tubulent kinetic energy

LES Large Eddy Simulation
$MINMOD$ Minimum Modulus
P Production Term
p Pressure
$PANS$ Partially Averaged Navier-Stokes
PIV Particle Image Velocimetry
$RANS$ Reynolds Averaged Navier-Stokes
S^+ Normalized streamwise distance
S_{ij} Resolved Stress tensor
$SMART$ Sharp and Monotonic Algorithm for Realistic Transport
U_τ Wall shear velocity
$URANS$ Unsteady Reynolds Averaged Navier-Stokes
v_i Velocity in i direction
x_i Distance in i direction
Y^+ Normalized wall normal distance

1
Introduction

As emission regulations grow more and more stringent the demand for lower fuel consumption increases. A large part of the energy wasted at higher velocities is due to air resistance; the air resistance at 100 km/h is up is up to 70% of the total resistance[1]. So in order to improve fuel consumption the drag is one of the factors that has to be improved. The total drag of the vehicle also greatly affects the range of electric vehicles which is something that is becoming a larger issue with the increased use of electric vehicles. To improve the drag the external flow of the vehicle has to be investigated, which can be done with either flow simulations or wind tunnel testing of either part or full scale models. To allow for a faster and cheaper development of the aerodynamics of the car, simulations are most commonly used in the earlier phase of development. Higher accuracy of the simulations would allow for better prediction of flow structures early on and less development with expensive wind tunnel models.

1.1 Background

The traditional approach to fluid simulations for external aerodynamics has been steady state Reynolds Averaged Navier-Stokes (RANS) simulations which yield fairly accurate results with respect to global forces and is a cheaper alternative due to the relatively low computational cost. RANS simulations tend to not capture the smaller scale flow structures very well however due to the averaging nature of the simulations. To better capture the nature of the unsteady flow around vehicles a time resolved simulation has to be used. The two most common approaches to this are the Unsteady Reynolds Averaged Navier-Stokes (URANS) simulations that filter out a significant amount of the fluctuations and Large Eddy simulations (LES) that is much more expensive than URANS and is too expensive to be used in industry. This has resulted in hybrid models being developed that combine the best of both simulation approaches. The hybrid approach investigated in this thesis is the Partially Averaged Navier-Stokes(PANS) approach and is based on the work of S. Girimaji[4] and further development of B. Basara, S. Krajnovic, S. Girimaji et al.[5]

1.2 Objective

The objective of this thesis is to investigate the accuracy of the PANS-k-e-z-f model with respect to the flow field characteristics as well as global forces.

1.3 Limitations

This thesis will be limited to using PANS as implemented in AVL Fire. The model used will be the 20deg SAE Notchback reference body. The conditions of the simulation will be set to be similar as they were in the wind tunnel, which means a stationary floor with a 60mm boundary layer at the body and inlet velocity of 40m/s.

2

Theory

In this chapter the relevant theory for this thesis will be presented including some brief theory of fluid mechanics as well as CFD, turbulence modeling and some coefficients used for post-processing.

2.1 Governing Equations

There are two principal ways of simulating fluid dynamics, the Lattice Boltzmann method and the Navier-Stokes method. The one used here is the Navier-Stokes method where the fluid is considered to be a continuum. The governing equations are described below in brief and a more extensive description can be found in [7]

2.1.1 Continuity equation

The continuity equation describes the balance of mass in a given control volume and is as follows:

$$\frac{d\rho}{dt} + \frac{d\rho v_i}{dx_i} = 0 \tag{2.1}$$

air is usually considered incompressible for flows with a mach number lower than 0.3[7], equation 2.1 is thus reduced to the following formula since the density is constant in incompressible flow:

$$\frac{dv_i}{dx_i} = 0 \tag{2.2}$$

2.1.2 Momentum

This is the set of equations that is used to calculate the transport of momentum in CFD[7]:

$$\rho\frac{dvi_i}{dt} = -\frac{\partial P}{\partial x_i} + \frac{\partial \tau_{ji}}{\partial x_j} + \rho f_i = -\frac{\partial P}{\partial x_i} + \frac{\partial}{\partial x_j}\left(2\mu S_{ij} - \frac{2}{3}\mu\frac{\partial v_k}{\partial x_k}\delta_{ij}\right) + \rho f_i \tag{2.3}$$

Which for incompressible flow with constant μ as well as neglecting body forces can be simplified to:

$$\rho\frac{dv_i}{dt} = -\frac{\partial P}{\partial x_i} + \mu\frac{\partial^2 v_i}{\partial x_j \partial x_j} \tag{2.4}$$

2.2 Computational Fluid Dynamics, CFD

2.2.1 Discretization

We define the normalized variable $\bar{\phi}$ as was proposed by Leonard [2] as:

$$\bar{\phi} = \frac{\phi - \phi_U}{\phi_D - \phi_U} \tag{2.5}$$

To investigate the boundedness of the discretizations we introduce the TVD constraint which is defined: [13]

$$\begin{cases} \bar{\phi}_f \leq 1 \text{ and } \bar{\phi}_f \leq 2\bar{\phi}_C \text{ and } \bar{\phi}_f \geq \bar{\phi}_C, & \text{if } 0 < \bar{\phi}_C < 1 \\ \bar{\phi}_f = \bar{\phi}_C & \text{if } \bar{\phi}_C \leq 0 \text{ or } \bar{\phi}_C \geq 1 \end{cases}$$

Another boundedness constraint based on the physical characteristics of the boundedness problem was set by Gaskell and Lau[13] as follows:

$$\begin{cases} \bar{\phi}_f \leq \ \text{ and } \bar{\phi}_f \geq \bar{\phi}_C, & \text{if } \ < \bar{\phi}_C < 1 \\ \bar{\phi}_f = \bar{\phi}_C & \text{if } \bar{\phi}_C \leq 0 \text{ or } \bar{\phi}_C \geq 1 \end{cases}$$

Central Differencing

Central Differencing tends to be very non-diffusive and accurate but does tend to generate instabilities and oscillations[11], it is defined as follows in AVL:

$$\phi_w = \frac{\phi_P + \phi_W}{2} \tag{2.6}$$

and the same is valid for the other faces with respective points.

MINMOD

MINMOD or the minimum modulus is a composite scheme based on the normalized variable formulation as described in [12]. The formulation of the MINMOD discretization scheme is as follows in the normalized variable formulation[15]:

$$\begin{cases} \bar{\phi}_f = \frac{3}{2}\bar{\phi}_C & \text{for } 0 < \bar{\phi}_C < \frac{1}{2} \\ \bar{\phi}_f = \frac{1}{2}(1 - \bar{\phi}_C) & \text{for } \frac{1}{2} < \bar{\phi}_C < 1 \\ \bar{\phi}_f = \bar{\phi}_C & \text{elsewhere} \end{cases}$$

The minmod scheme was developed to be bounded, accurate and have low numerical dissipation. The full derivation and description can be found in [12]

SMART

SMART, Sharp and Monotonic Algorithm for Realistic Transport, is a discretization scheme developed using the technique called curvature compensation and is designed to have a high order of accuracy and be bounded.

The normalized values are calculated as described in [13]:

$$\bar{\phi}_{i-1/2} = (\frac{3}{4} + 2\alpha^-)\bar{\phi}_{i-1} + (\frac{3}{8} + \alpha^-) \tag{2.7}$$

where α^- is calculated as follows

$$\alpha^- = \left[\frac{\bar{\phi}_{i-1/2} - \frac{3}{8}(2\bar{\phi}_{i-1} + 1}{2\bar{\phi}_{i-1} - 1}\right] \tag{2.8}$$

and,

$$\begin{cases} \bar{\phi}_{i-1/2} = 3\bar{\phi}_{i-1} & \text{for } 0 < \bar{\phi}_C < \frac{1}{6} \\ \bar{\phi}_{i-1/2} = \frac{3}{8}(2\bar{\phi}_{i-1} + 1) & \frac{1}{6} < \bar{\phi}_C \le \frac{5}{6} \\ \bar{\phi}_{i-1/2} = 1 & \text{for } \frac{5}{6} < \bar{\phi}_C < 1 \\ \bar{\phi}_{i-1/2} = \bar{\phi}_{i-1} & \text{elsewhere} \end{cases}$$

From numerical experiments in [13] it can be seen that the SMART discretization is as good or better than the QUICK discretization at predicting sharp gradients and is bounded unlike the quick scheme. From the numerical experiments in [15] it can also be seen that the SMART scheme is far less dissipative than the MINMOD scheme.

The way these are implemented in AVL fire is as is described below. For further information see the AVL Fire manual[3]:
First an interpolation factor is defined as:

$$f_f = \frac{|\vec{r}_{P_j} - \vec{r}_f|}{|\vec{r}_f - \vec{r}_P| + |\vec{r}_{P_j} - \vec{r}_f|} \tag{2.9}$$

a flow oriented interpolation factor is then introduced as:

$$f_f^* = \begin{cases} 1 - f_f & if \dot{m}_j \ge 0 \\ f_f & if \dot{m}_j < 0 \end{cases}$$

the general upstream-weighted approximation is defined as

$$\phi_f = \phi_C + \Big[(1/2)f_f^*(1+f_f^*) - \alpha_f\Big](\phi_D - \phi_C) + \Big[(1/2)f_f^*(1+f_f^*) - \alpha_f\Big](\phi_C - \phi_U) \tag{2.10}$$

The limiter argument is then introduced from eq 2.5 as:

$$\varphi_f^* = \frac{\bar{\phi}_C}{1 - \bar{\phi}_C} \tag{2.11}$$

equation 2.10 can then be simplified as:

$$\bar{\phi}_f = \bar{\phi}_c + \varphi_f(1 - \bar{\phi}_c) \tag{2.12}$$

where φ_f is a function of φ_f^* as follows:

$$\varphi_f = \Big[(1/2)f_f^*(1 + f_f^*) - \alpha_f\Big] + \Big[(1/2)f_f^*(1 - f_f^*) + \alpha_f\Big]\varphi_f^* \tag{2.13}$$

and φ_f is defined as:

$$\varphi_f = \begin{cases} f_f^* max\Big\{0, min\Big(\varphi_f^*, 1\Big)\Big\} & \text{for MINMOD} \\ max\Big\{0, min\Big[\beta_1\varphi_f^*, 0.5f_f^*(1+f_f^*) + 0.5f_f^*(1-f_f^*)\varphi_f^*, \beta_2\Big]\Big\} & \text{for SMART} \end{cases}$$

2.2.2 Turbulence Modeling

PANS

PANS is a hybrid formulation between DNS and URANS where the cut-off filtering is variable and adapts to how much filtering is needed in each cell. This gives it the benefit of resolving fluctuations where possible and filtering out fluctuations where it is not possible to resolve them[4]. The PANS model implemented in AVL Fire is the PANS $k-\varepsilon-\zeta-f$ which is a variation of the v^2-f model[5].

By partially averaging the governing equations we get:

$$\frac{\partial \bar{v}_i}{\partial x_i} = 0 \tag{2.14}$$

$$\frac{\partial \bar{v}_i}{\partial t} + \frac{\partial(\bar{v}_i\bar{v}_j)}{\partial x_i} = -\frac{1}{\rho}\frac{\partial \bar{p}}{\partial x_i} + \frac{\partial}{\partial x_j}\Big(\nu\frac{\partial \bar{v}_i}{\partial x_j} - \tau_{ij}\Big) \tag{2.15}$$

where, $\mathcal{P}$ is the partial averaging operator:

$$\tau_{ij} = (\mathcal{P}(v_iv_j) - \bar{v}_i\bar{v}_j) \tag{2.16}$$

Choosing a Boussinesque constitutive relation to close our model τ_{ij}, also called the second-order moment, can be written as:

$$\tau_{ij} = -2\nu_u S_{ij} + \frac{2}{3}k_u\delta_{ij} \tag{2.17}$$

The unresolved kinetic energy and dissipation gives the eddy viscosity as

$$\nu_u = c_\mu\frac{k_u^2}{\varepsilon_u} \tag{2.18}$$

and the resolved stress tensor is given as

$$S_{ij} = \frac{1}{2}\Big(\frac{\partial v_i}{\partial x_j} + \frac{\partial v_j}{\partial x_i}\Big) \tag{2.19}$$

Models for the system of equations given are derived in [4] as:

$$\frac{\partial k_u}{\partial t} + v_j\frac{\partial k_u}{\partial x_j} = P_u - \varepsilon_u + \frac{\partial}{\partial x_j}\Big(\frac{\nu_u}{\sigma_{k_u}}\frac{\partial k_u}{\partial x_j}\Big) \tag{2.20}$$

$$\frac{\partial \varepsilon_u}{\partial t} + v_j\frac{\partial \varepsilon_u}{\partial x_j} = C_{\varepsilon 1}P_u\frac{\varepsilon_u}{k_u} - C^*_{\varepsilon 2}\frac{\varepsilon_u^2}{k_u} + \frac{\partial}{\partial x_j}\Big(\frac{\nu_u}{\sigma_{\varepsilon_u}}\frac{\partial \varepsilon_u}{\partial x_j}\Big) \tag{2.21}$$

where the model coefficeints are:

$$C^*_{\varepsilon 2} = C_{\varepsilon 1} + \frac{f_k}{f_\varepsilon}(C_{\varepsilon 2} - C_{\varepsilon 1}); \quad \sigma_{k_u} = \sigma_k \frac{f_k^2}{f_\varepsilon}; \quad \sigma_{\varepsilon_u} = \sigma_\varepsilon \frac{f_k^2}{f_\varepsilon} \tag{2.22}$$

the two coefficients that control the filter cut off are f_k and f_ε and are defined as

$$f_k = \frac{k_u}{k}, \qquad f_\varepsilon = \frac{\varepsilon_u}{\varepsilon} \tag{2.23}$$

assume $f_\varepsilon = 1$ because the mesh used is assumed to have a cut off in the energy containing or inertial scales meaning that we have not resolved any of the dissipative scales and thus $\varepsilon_u = \varepsilon$.

f_k is dependant on the following inequality and means that the model cut off is allowed to be larger than the grid but not smaller. Δ is the geometric-average grid cell dimension ($\Delta = (\Delta_x \times \Delta_y \times \Delta_z)^{\frac{1}{3}}$) and Λ is the integral length scale:

$$f_k \geq \frac{1}{c_\mu}\left(\frac{\Delta}{\Lambda}\right)^{\frac{1}{2}}, \qquad \Lambda = \frac{k^{\frac{2}{3}}}{\varepsilon} \tag{2.24}$$

Further description of the derivation of the model can be found in [5] and the complete PANS $k - \varepsilon - \zeta - f$ model is given by:

$$\nu_u = C_\mu \zeta_u \frac{k_u^2}{\varepsilon_u} \tag{2.25}$$

$$\frac{\partial k_u}{\partial t} + v_j \frac{\partial k_u}{\partial x_j} = P_u - \varepsilon_u + \frac{\partial}{\partial x_j}\left(\frac{\nu_u}{\sigma_{k_u}} \frac{\partial k_u}{\partial x_j}\right) \tag{2.26}$$

$$\frac{\partial \varepsilon_u}{\partial t} + v_j \frac{\partial \varepsilon_u}{\partial x_j} = C_{\varepsilon 1} P_u \frac{\varepsilon_u}{k_u} - C^*_{\varepsilon 2} \frac{\varepsilon_u^2}{k_u} + \frac{\partial}{\partial x_j}\left(\frac{\nu_u}{\sigma_{\varepsilon_u}} \frac{\partial \varepsilon_u}{\partial x_j}\right) \tag{2.27}$$

$$\frac{\partial \zeta_u}{\partial t} + v_j \frac{\partial \zeta_u}{\partial x_j} = f_u - \frac{\zeta_u}{k_u}\varepsilon_u(1 - f_k) + \frac{\partial}{\partial x_j}\left(\frac{\nu_u}{\sigma_{\zeta_u}} \frac{\partial \zeta_u}{\partial x_j}\right) \tag{2.28}$$

$$L_u^2 \Delta^2 f_u - f_u = \frac{1}{T_u}\left(c_1 + C_2 \frac{P_u}{\varepsilon_u}\right)\left(\zeta_u - \frac{2}{3}\right) \tag{2.29}$$

with the constants as follows:

$$\sigma_{k_u} = \sigma_k \frac{f_k^2}{f_\varepsilon}, \quad \sigma_{\varepsilon_u} = \sigma_\varepsilon \frac{f_k^2}{f_\varepsilon}, \quad \sigma_{\zeta_u} = \sigma_\zeta \frac{f_k^2}{f_\varepsilon} \quad C_\mu = 0.22, \quad c_1 = 0.4, \quad c_2 = 0.65, \quad C_{\varepsilon 2} = 1.9 \tag{2.30}$$

$$T_u = max\left[\frac{k_u}{\varepsilon}, C_\tau\left(\frac{\nu}{\varepsilon}\right)^{\frac{1}{2}}\right], \quad L_u = C_L max\left[\frac{k^{\frac{3}{2}}}{\varepsilon}, C_\eta\left(\frac{\nu^3}{\varepsilon}\right)^{\frac{1}{4}}\right] \tag{2.31}$$

where $C_L = 0.36$ and $C_\tau = 6.0$ and $C_{\varepsilon 1} = 1.4(1 + 0.045/\sqrt{\zeta_u})$

2.3 Important Coefficients

2.3.1 Q-invariant

To define vortices we must have a criterion for what a vortex is. One way of doing this was established in [8] and is defined as an area where the irrotational straining is small compared to the vorticity. This is described here with the second invariant of the deformation tensor being smaller than a negative threshold value,

$$II < -II_E \qquad II = \frac{\partial v_i}{\partial x_j}\frac{\partial v_j}{\partial x_i} = E_{ij}^2 - \frac{1}{2}\omega_i^2 \tag{2.32}$$

where E_{ij} is the symmetric strain tensor $\frac{1}{2}\Big(\frac{\partial v_i}{\partial x_j} + \frac{\partial v_j}{\partial x_j}\Big)$ and $\epsilon_{ijk}\frac{\partial v_k}{\partial x_j}$ is the vorticity.

The Q-criterion is however usually described as $Q = -II$ and then set as greater than a threshold value, thus

$$Q = \frac{1}{2}\Bigg(\Big(\epsilon_{ijk}\frac{\partial v_k}{\partial x_j}\Big)^2 - \Big(\frac{\partial v_i}{\partial x_j} + \frac{\partial v_j}{\partial x_j}\Big)^2\Bigg) \tag{2.33}$$

2.3.2 Coefficient of pressure

The coefficient of pressure is a dimensionless number used to describe the relative pressure in a flow field and enables a comparison of flows of different velocities and size of body. It is defined as [7]:

$$C_p = \frac{p - p_\infty}{\frac{1}{2}\rho_\infty V_\infty^2} \tag{2.34}$$

2.3.3 CFL condition

CFL is a condition used to gauge the temporal resolution and stability for a given mesh. The CFL condition is defined as [9]

$$C = max\Big(\frac{v_x \Delta t}{\Delta x}, \frac{v_y \Delta t}{\Delta y}, \frac{v_z \Delta t}{\Delta z}\Big) \tag{2.35}$$

where v is the velocity, Δt is the time step and $\Delta x, y, z$ is the cell distance.
For an implicit time marching scheme the CFL number has to be less than one, but for an explicit scheme which is used in this thesis the condition is not as strict. It can however affect the results so the CFL number was kept as close to 1 as possible without increasing the simulation time too much.

2.3.4 y^+

The dimensionless wall distance y+ is defined as [7]:

$$y^+ = \frac{y u_\tau}{\nu} \tag{2.36}$$

with

$$u_\tau = \sqrt{\frac{\tau_w}{\rho}} \tag{2.37}$$

This is used to define where in the boundary layer a point is and in conjunction with the distance to the first cell center is used to define how well the boundary layer is resolved. The model used in this thesis uses a hybrid wall treatment which means that the y+ value does not have to be a specific value for it to work but since accurate results are sought after a low y+ of 1 is targeted to better predict the boundary layer and thus increase accuracy with respect to the point of separation for example.

3

Methods

3.1 Wind tunnel data

The wind tunnel data was obtained from the Loughborough University ¼ scale wind tunnel and presented in [10] as well as published online for evaluation of numerical methods.

3.1.1 PIV

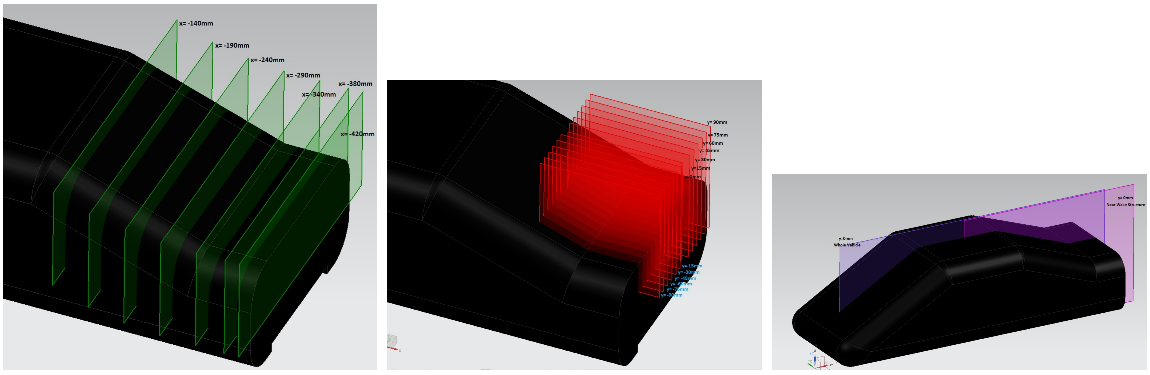

(a) Rear notch spanwise **(b)** Rear notch streamwise **(c)** center line

Figure 3.1: Figures displaying location of planes.

Velocity data for the SAE reference body was obtained by PIV. The images were captured with a 2048x2048 resolution and a 1mm thick laser sheet with an inter-frame time optimized for each case so that the average pixel shift was 1/4 of the final interrogation window size. To generate the vector fields a multi pass approach was used with an inital size of 128x128 pixels and used to shift the cells as the size was reduced to a final size of 32x32 pixels. To increase the number of vectors in the field an overlap of the interrogation cells of 50% was used. The velocity field was then validated automatically and invalid vectors were removed and subsequently replaced with vectors using either the second strongest correletaion peak or linear interpolation to avoid missing or zero values in the wrong places. A total number of 1000 instantaneous vector fields were used to create a mean flow vector field for each plane. The velocity in the freestream has an accuracy of $\pm 0.2\%$ that decreases to $\pm 2\%$ in the wake.

The Data was downloaded in tables for each of the planes and was processed in Matlab to order it into matrices and export the coordinates to a .CSV file so that data from matching locations could be extracted from the simulation data through EnSight using Python. This was then imported into Matlab again and sorted again to ensure the accuracy of the plots.

3.1.2 Pressure probes

In the SAE reference body case pressure points were collected on the backlight, bootdeck, base and along the center line. This was done with flush fitted 0.9mm I.D tubes via small bore flexible tubung to two 64-channel scanners with an accuracy of $\pm$1.47Pa. A more exact description of the measurement method and probe placement can be found in [10].

3.2 Simulation setup

General Setup

To be able to compare the data from the simulations to the data acquired in wind tunnel test by Wood, D., Passmore, M., and Perry, A. [10] the simulation setup has to match the conditions of the wind tunnel. Due to the stationary floor of the wind tunnel used in [10] an inlet velocity profile has to be set to match the conditions measured at the body. This was done by setting a turbulent velocity profile with the height of 26 mm at the inlet to let the boundary layer height to grow to 60mm at the front of the body as was specified in [10]. To match the wind tunnel conditions a no slip stationary wall boundary condition is applied to the floor and body while the sides and roof are set as symmetric boundary conditions. Further the height and width of the simulation domain was set to be equal to the dimensions of the wind tunnel to match eventual blockage effects in the wind tunnel which is 1.92m wide and 1.32m tall. The length of the wind tunnel was set to 6.64m with 1.4m upstream of the body and 4.4m downstream, equating to 1.7 car lengths upstream and 5.25 car lengths downstream to minimize the effect of boundaries upstream and downstream while maintaining a low cell count. Multiple discretization schemes were tried to investigate the difference, for continuity a CD scheme was used and MINMOD for turbulence in all simulations and for momentum both the MINMOD and AVL SMART schemes were used. The time step was set to 3e-5s to keep the CFL number below one.

Mesh

To resolve the boundary layer a target y^+ value of 1 was targeted. To achieve this while maintaining a low cell count it was chosen to use 10 boundary layer cells with a growth rate of 1.8 and a total thickness of 1.5mm. The surface cell size of the body was set to 2mm to generate a smooth surface and a resolved enough flow near the body. The refinement depth was set to 50mm to resolve the flow close to the body where the effect of mesh resolution is most important. To give a smooth mesh around the support pillars the mesh surface size there is set to 0.5mm. To resolve the wake structures to a satisfactory degree two refinement regions were created behind the car with 4mm and 8mm cell size. Due to the way that refinements are implemented in the Fire M Fame poly mesher the width of the refinements became too wide when an appropriate height was chosen. The height was set to 330mm to cover the full wake of the body. The mesh cell count is 17.8 million cells and could most likely be reduced to around 14 million with better refinement shapes maintaining the same accuracy. To reduce the total cell count a target cell size in the far field was chosen as 70mm.

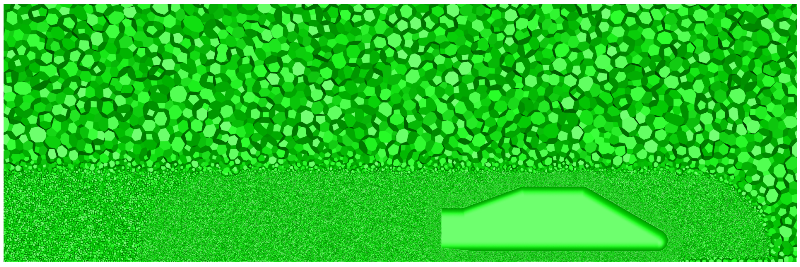

Figure 3.2: Figure showing the mesh with refinement regions.

4

Results

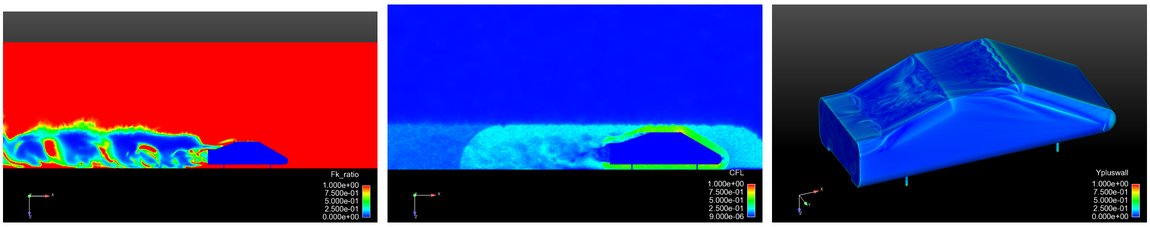

(a) F_k (b) CFL (c) Y^+

Figure 4.1: Figures displaying temporal and spatial resolution of the simultaion. The plane is a XZ plane at Y=0. All three are graded from 0 to 1.

To gauge the quality and fidelity of the simulation a few parameters have been chosen to demonstrate this. The fidelity of the simulation can be well described by the F_k ratio since this is based on the amount of turbulence that is resolved. As can be seen in figure 4.26a the wake of the car is well resolved when it comes to turbulent fluctuations. To gauge if the mesh is fine enough close to the surface to be able to use a low Reynolds number model close to the surface the non-dimensional wall distance Y^+ is used and as can be seen in figure 4.26c is far below 1 and should give a well resolved viscous sublayer of the boundary layer. Even though an implicit scheme is used the CFL number was kept as low as possible which can be seen in figure 4.26b to be under 1 in most places except along the edges of the roof. With the Resolution parameters as they are it can be assumed that the mesh and time step is of sufficient size.

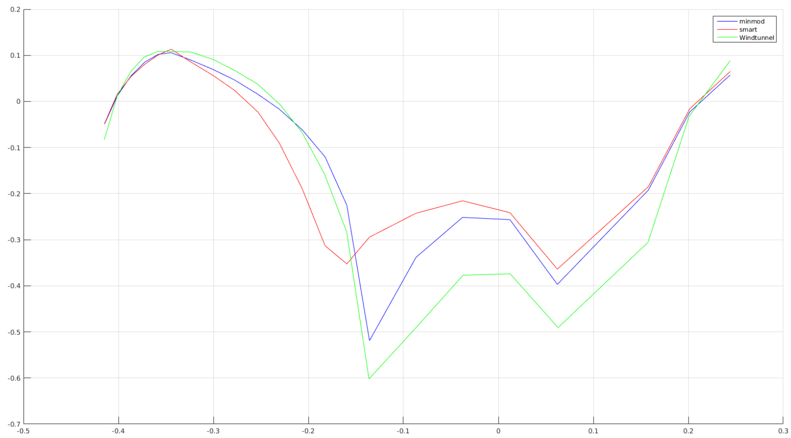

Figure 4.2: Graph of C_p vs x on the top of the body.

Figure 4.2 shows fairly good agreement with magnitude between simulation and wind tunnel data and very good agreement regarding shape and position of peaks.

4.1 MINMOD simulation

The results of this simulation in terms of drag and lift are not good with respect to the drag, being 5.35% lower, and very poor with respect to lift with the values being 179.5% higher than those of the experimental values.

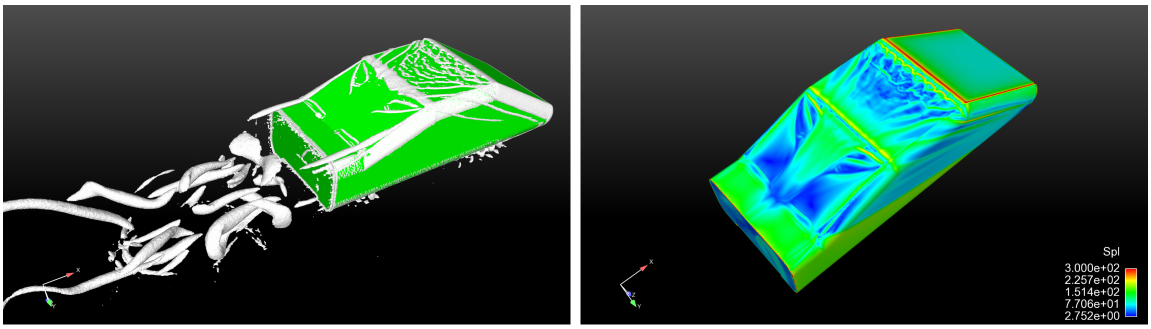

(a) Q-critereon at 800 000

(b) Spanwise and streamwise resolution S^+

Figure 4.3: Figure of resolved structures and specific resolution for the minmod simulation.

As can be seen in figure 4.3 there is a significant amount of flow structures resolved. The resolution in the spanwise and streamwise direction is not good enough for LES but is fairly good and in most areas where the separation occurs is below around 150. As can be seen in figure 4.26a the wake of the body is fairly well resolved with there being no separated flow along the backlight and it thus having a high F_k value there.

Flow field

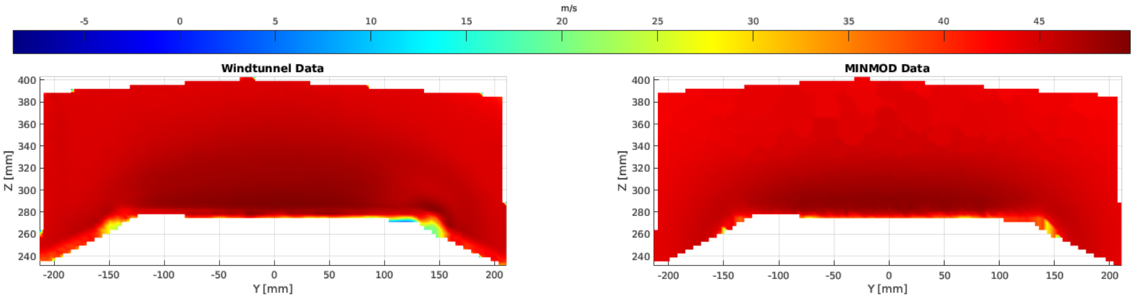

Figure 4.4: YZ plane at x=-140mm, showing flow magnitude in X direction.

As can be seen in figure 4.4 the flow field of the MINMOD simulation is very similar to that of the experiment except for along the C-pillars where the velocity is lower in the experiment than it is in the simulation.

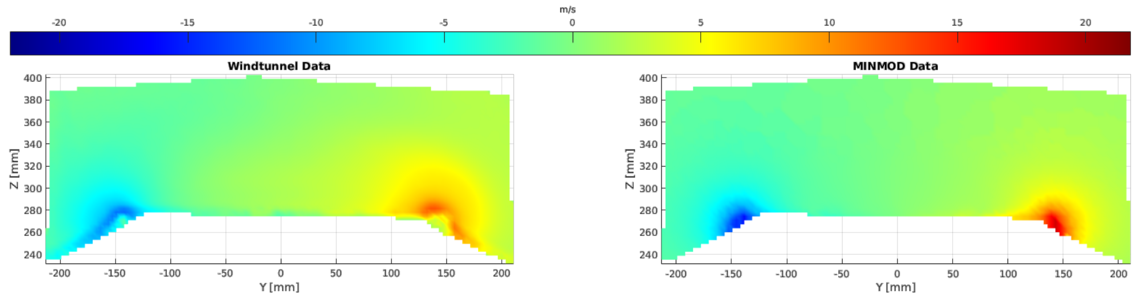

Figure 4.5: YZ plane at x=-140mm, showing flow magnitude in Y direction.

In Figure 4.5 we can see that the crossflow over the C-pillars of the simulation has a much smaller area and the gradient outwards is higher than in the experiment.

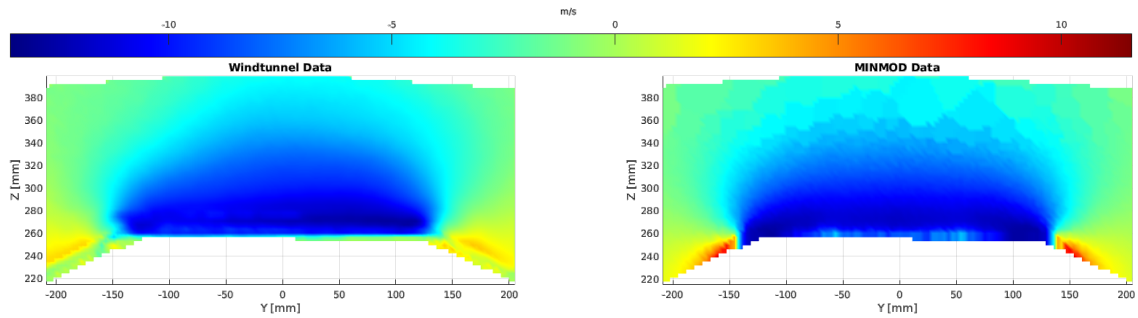

Figure 4.6: YZ plane at x=-190mm, showing flow magnitude in Z direction..

As can be seen in figure 4.6 the downwards flow along the backlight is very well matched between the simulation and the experiments. There is however a discrepancy at the C-pillar where the velocity is higher in the simulation than the experiments. The downwards flow is also slightly wider in the simulation than it is in the experiment. A slight asymmetry can be seen in the experimental data which is not present in the simulation.

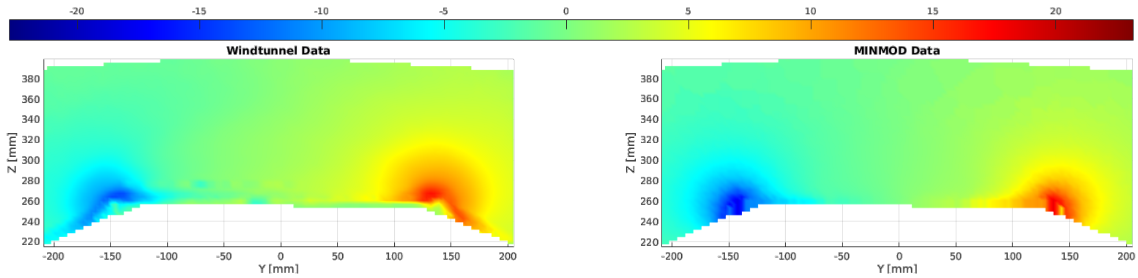

Figure 4.7: YZ plane at x=-190mm, showing flow magnitude in Y direction..

In figure 4.7 it should be noted that the location and shape of the flow structures are similar between the experiment and simulation but the magnitude is different. It can be seen that the larger gradient in the simulation gives a smaller area of high velocity. There is also asymmetry present in the experimental data which is not present in the simulation. The asymmetry mentioned here is the size of the high velocity areas over the C-pillars where the area at Y=140 is taller and larger than that of the one at Y=-140.

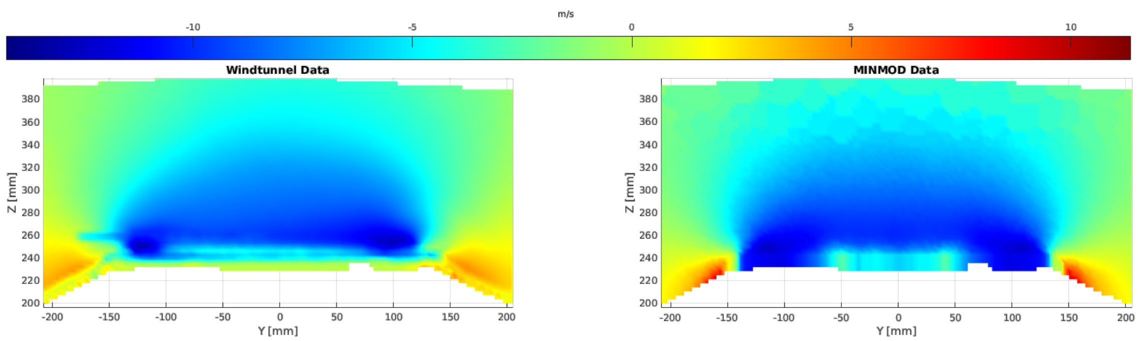

Figure 4.8: YZ plane at x=-240mm, showing flow magnitude in Z direction.

In figure 4.8 the difference between the simulation and experiment can quite clearly be seen along the center of the backlight where the area of separated flow is much narrower in the simulation than in the experiment and the separation as well as downwards flow is also not symmetric in the experiment, which it is in the simulation. It can also be seen that the upwards flow, positive values in figure 4.8, is over a larger area outside the C-pillars higher up in the experiments than in the simulation. The largest asymmetry of the experimental data is the bulk downwards flow where the top of it is very clearly skewed towards the y>0 side, this asymmetry is not present in the simulation.

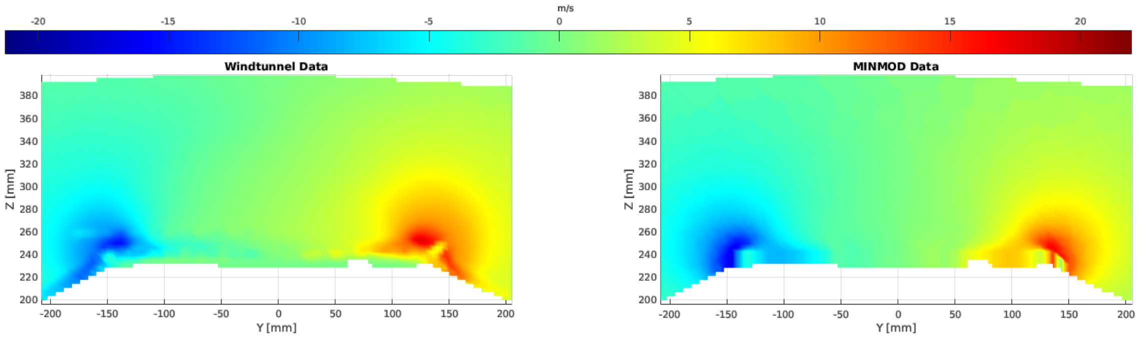

Figure 4.9: YZ plane at x=-240mm, showing flow magnitude in Y direction.

Figure 4.9 shows the flow to be very similar between the simulation and experiment except for a greater magnitude and area of crossflow towards the center line close to the surface. The same difference in gradient away from the high velocity zones that was seen in other planes is also present here. There is also a slight difference at around Y=-180 and Y=170 where there is a larger stretched out part with higher velocity in the experimental data then there is in the simulation.

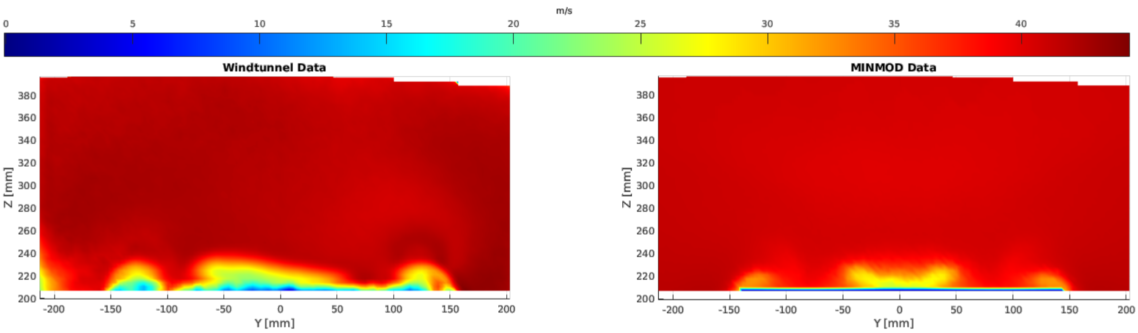

Figure 4.10: YZ plane at x=-420mm, showing flow magnitude in X direction.

Figure 4.10 shows a very clear asymmetry that is present in the experimental data but not present in the simulation in the area from Y=-150 to Y=-100. Where the vortices seen in figure 4.11 are located it can be seen that the X velocity is much lower in the experiments than it is in the simulations.

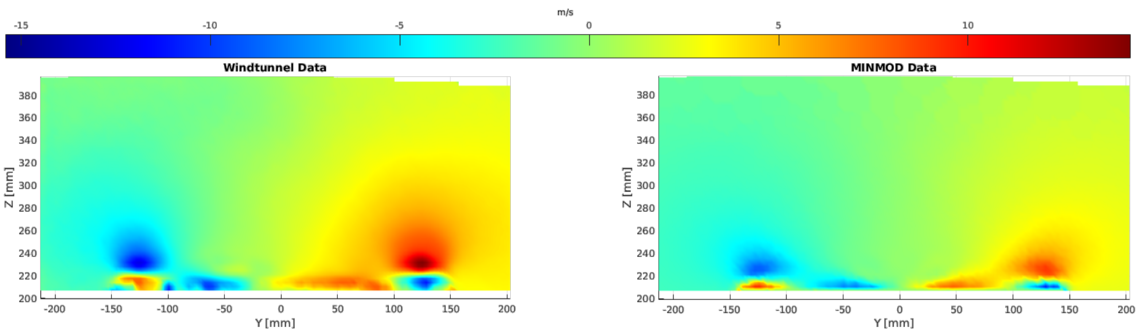

Figure 4.11: YZ plane at x=-420mm, showing flow magnitude in Y direction.

Figure 4.11 shows the location of the vortices as well as the strength and gives an indication about the size. It can be seen that the vortex location is very similar between the simulation and experimental data. There is also some crossflow present in both the simulation and experiment. However the size and strength of the vortices is poorly predicted where the experimental ones are much stronger and larger than those of the simulation. The location and strength of the crossflow is not well predicted either. It is much weaker in the simulation than it is in the experimental data.

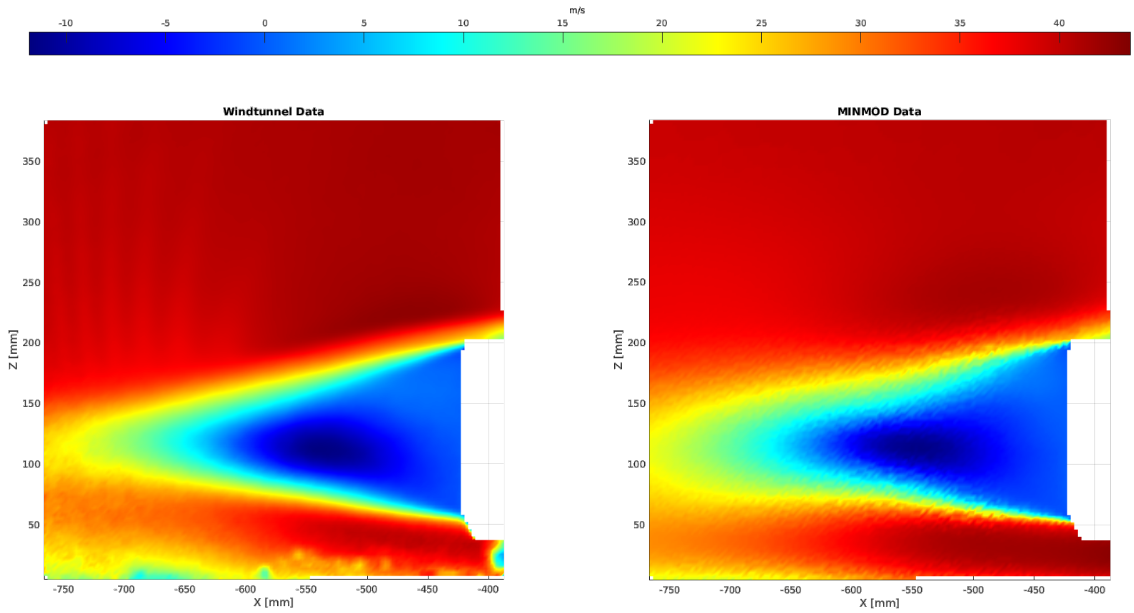

Figure 4.12: XZ plane at y center line, showing flow magnitude in X direction.

Figure 4.12 Shows the base wake and as can be seen the closing of the innermost two contours is fairly well predicted but the total wake is much longer at the end of the figure in the simulation than it is in the experimental data. The internal area of forwards flow (negative velocity magnitude) around X= -550 and Y=125 is well predicted in magnitude, shape and size. The flow from underneath the body seems to be not as attached in the simulation as it is in the experiment and adds to the delayed closing of the wake. There is a distinct change in the high velocity flow coming from the diffuser at X=-560 in both data sets but in the simulation data it takes a much sharper turn downwards than it does in the experimental data where it only slightly diverts downwards and continues to close the wake, which it does not in the simulation.

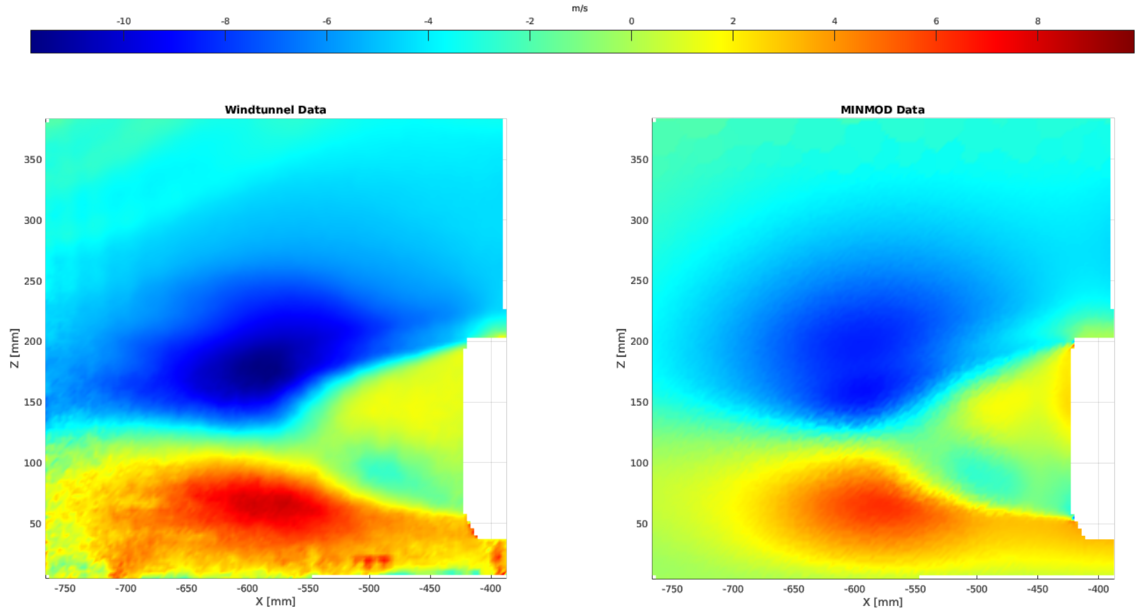

Figure 4.13: XZ plane at y center line, showing flow magnitude in Z direction.

Figure 4.13 shows very similar contours when it comes to the base wake close to the body. The internal shapes of the base wake are very well represented and the positive and negative velocity areas are fairly well predicted, however with the wrong magnitude, forwards of X=-610. Further downstream the flow prediction is poor where there is no longer a clear distinction between the top and bottom portion of the wake which there is in the experimental data. This also indicates that the wake closure rate should differ behind X=-610 which can indeed be seen in Figure 4.12.

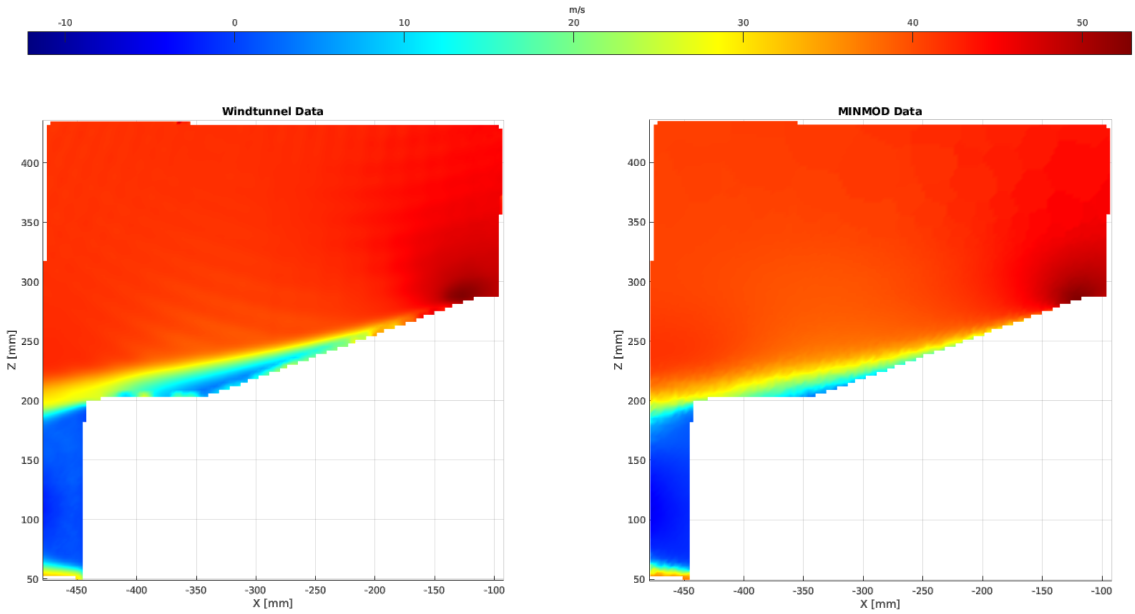

Figure 4.14: XZ plane at y center line, showing flow magnitude in X direction.

Figure 4.14 shows that along the center line there is a large bubble of separation in the experiment as well as separating at about 1/3 down along the backlight from the roof. In the simulation it separates further down the backlight at about 60% of the length down from the roof. It should also be noted that due to the later point of separation in the simulation there is a much stronger interaction between the shear layer at the top edge of the separation bubble and the rear most edge of the bootdeck. There is also a steeper closure angle at the top of the base wake in the simulation than there is in the experimental data.

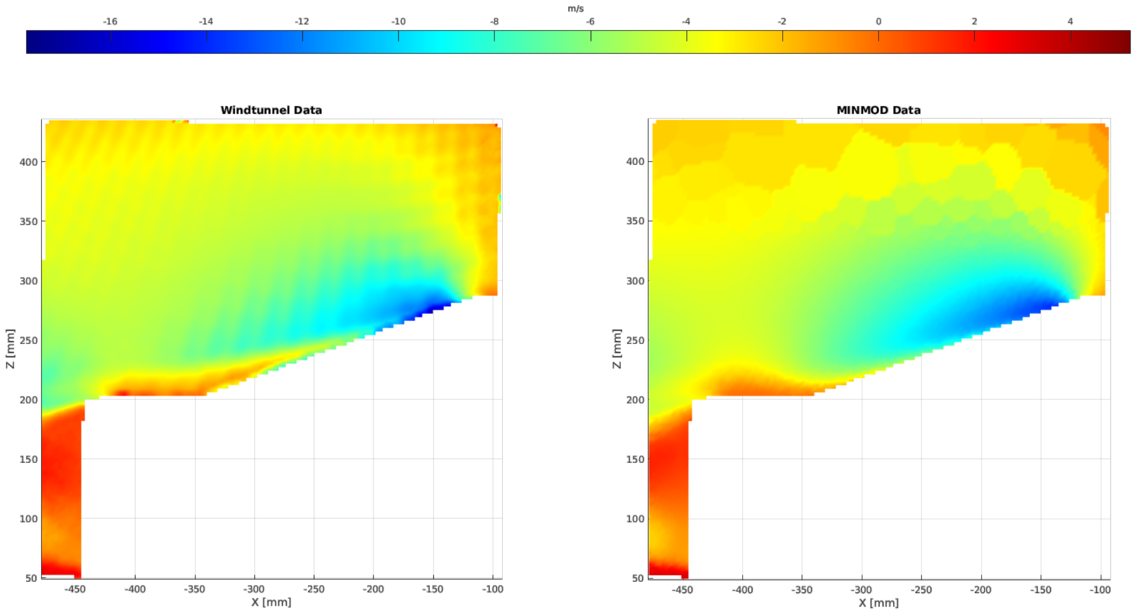

Figure 4.15: XZ plane at y center line, showing flow magnitude in Z direction.

Figure 4.15 Shows very clearly where the separation occurs and here it looks like the separation is occurring very gradually in the case of the simulation compared to the experiment. In the experiment there seems to be a very sharp edge where it transitions from fully attached to fully detached at X=-220. For the simulation the same transition seems to occur between x=-160 and x = -250. The top of the base wake is again poorly predicted but the bottom and middle of the base wake is well predicted here.

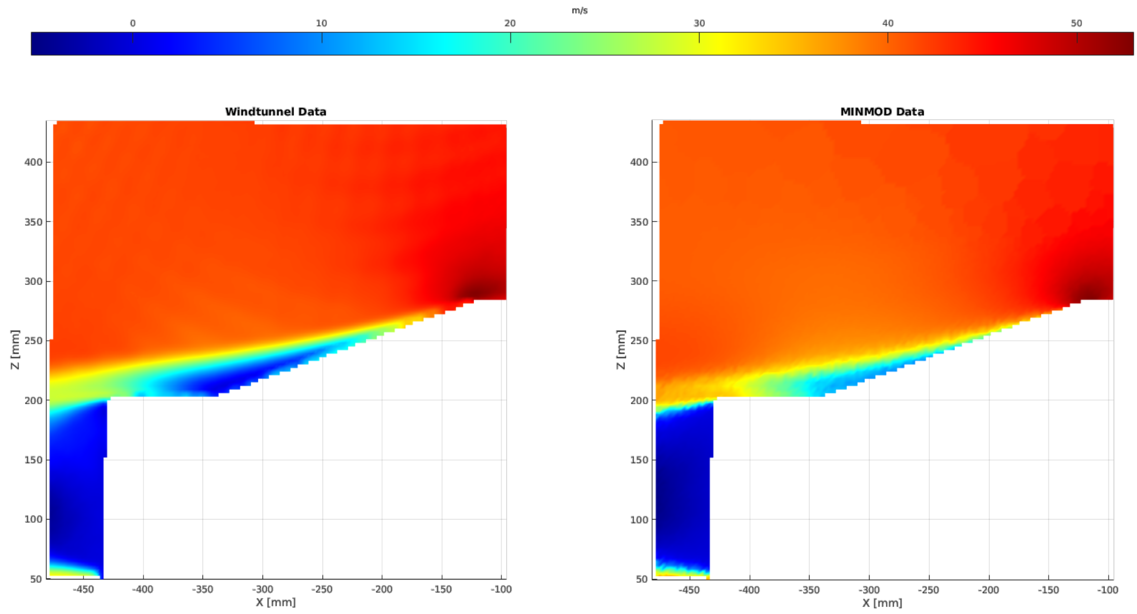

Figure 4.16: XZ plane at Y=-45mm, showing flow magnitude in X direction.

Figure 4.16 shows that the simulation predicts a too late point of separation and a much too small separation bubble. The experimental data shows a large area of practically stationary air compared to the same area of the simulation showing 40% of free stream velocity. The figure also shows a better captured shape of the base wake which is easily seen when comparing the top and bottom contours of the base wake to those of the experimental data.

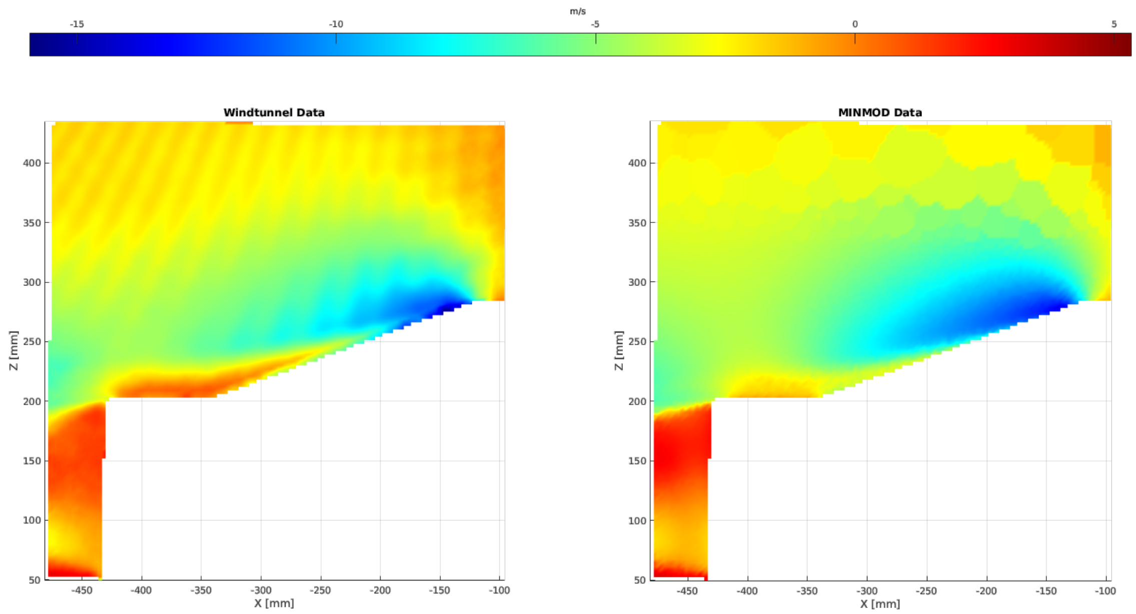

Figure 4.17: XZ plane at Y=-45mm, showing flow magnitude in Z direction.

Figure 4.17 shows the later point of separation but here there is a sharper point of separation compared to that in figure 4.15. However the flow in the simulation keeps a negative Z velocity all the way until the base of the body whereas the experiment shows an area with very small or no velocity in the Z direction over the bootdeck indicating stronger separation. The Z velocity of the base wake is again well captured at the bottom and middle but poorly predicted at the top of the base wake where the closure angle is wrong in the simulation.

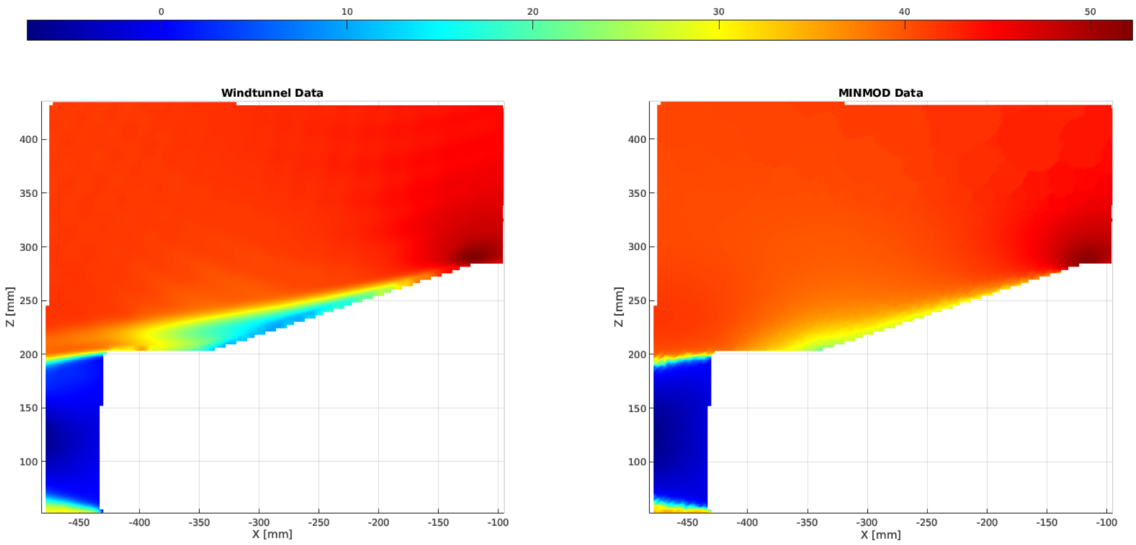

Figure 4.18: XZ plane at Y=-75mm, showing flow magnitude in X direction.

Figure 4.18 shows a larger difference when it comes to the area of separation. The simulation shows in essence no separation and the experimental data shows quite strong separation but with a separation bubble that is detached from the bootdeck indicating the crossflow that was seen in figure 4.11 closes the wake from the sides. The Base wake is well predicted at the top here but with a bit too shallow of an angle at the bottom compared to the experimental data.

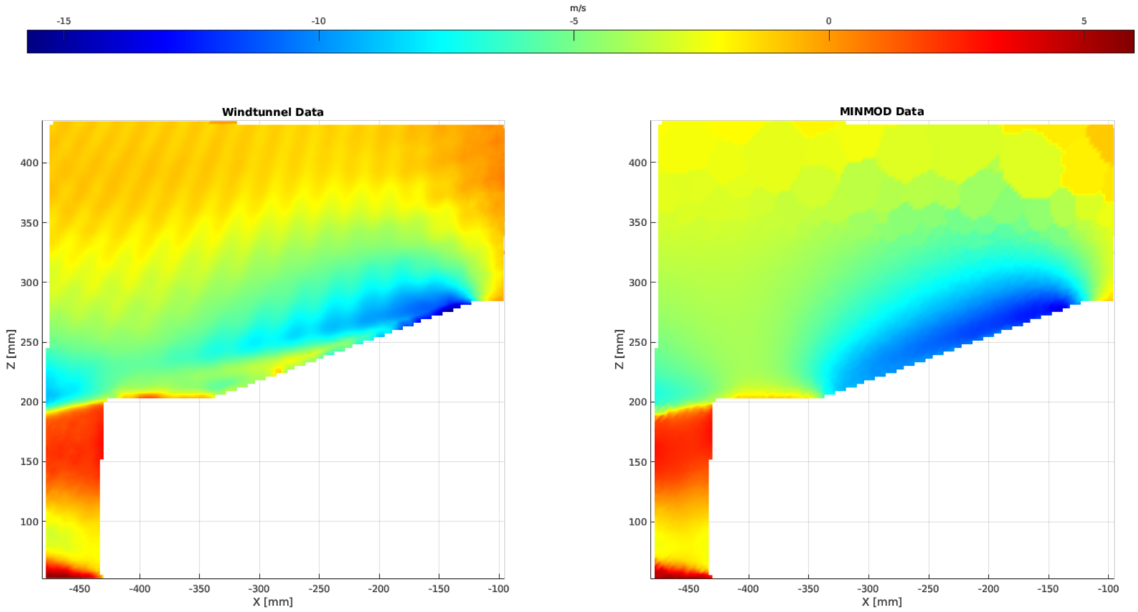

Figure 4.19: XZ plane at Y=-75, showing flow magnitude in Z direction.

Figure 4.19 shows what was indicated in figure 4.18 which is that the simulated flow stays attached along the entire backlight whereas the experimental data shows roughly the same point of separation as seen in previous planes. The Z velocity of the base wake is very well predicted in this plane. There is however a slight difference in the middle of the wake where the negative velocity area has a different shape.

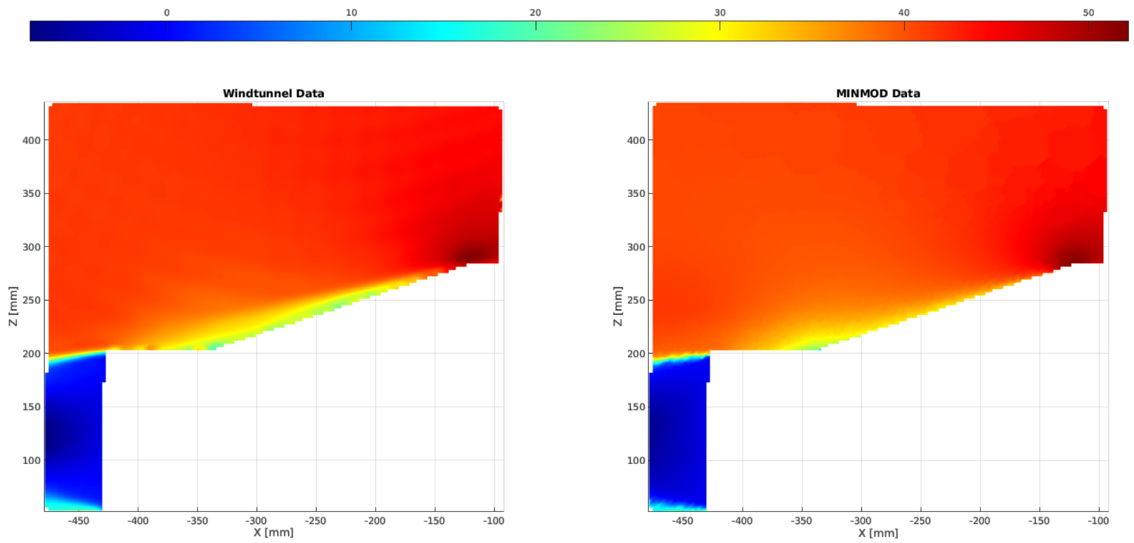

Figure 4.20: XZ plane at Y=-90mm, showing flow magnitude in X direction.

Figure 4.20 shows similar flow fields for both simulation and experiment but with significant differences close to the edge of the bootdeck and close to the roof. There is more separation and crossflow in the experiment compared to the simulation where there are no signs of separation along the roofline and a smooth interaction with the bootdeck in the simulation data.

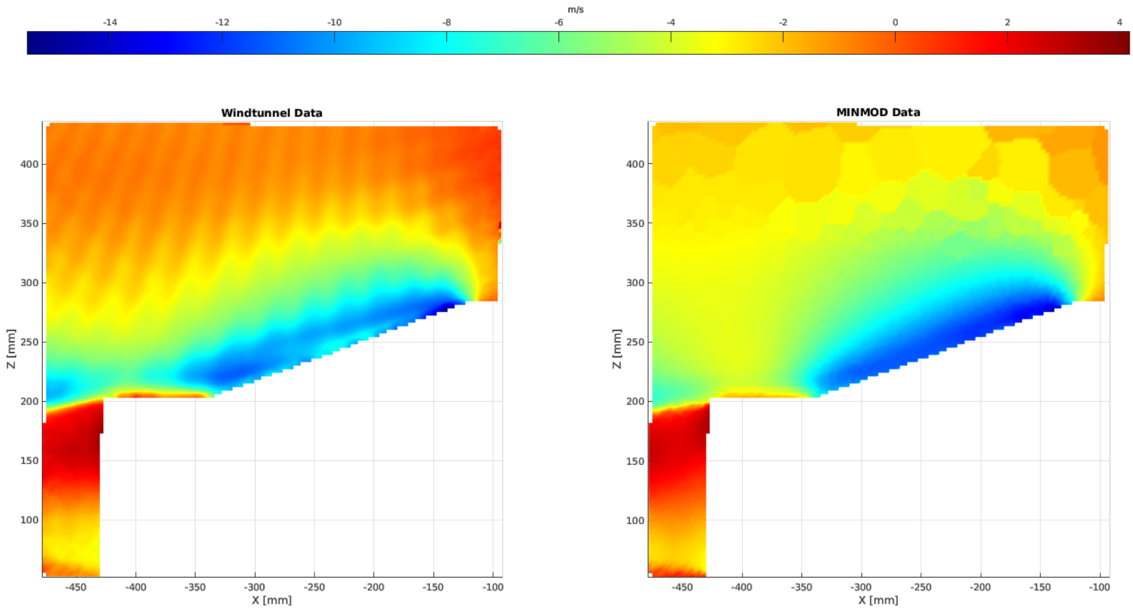

Figure 4.21: XZ plane at Y=-90, showing flow magnitude in Z direction.

Figure 4.21 shows no signs of separation on either of the data sets and would indicate that the area on the top of the backlight for the experiment as seen in figure 4.20 is something else than separation. The downward flow in the experimental data extends further out over the bootdeck than it does in the simulation which could explain the larger area of downwards flow over the base wake of the experiment compared to that of the simulation. The Z directional flow of the base wake matches very well with the only exception being the bottom of the base wake where the area of negative velocity is too small.

Pressure Data

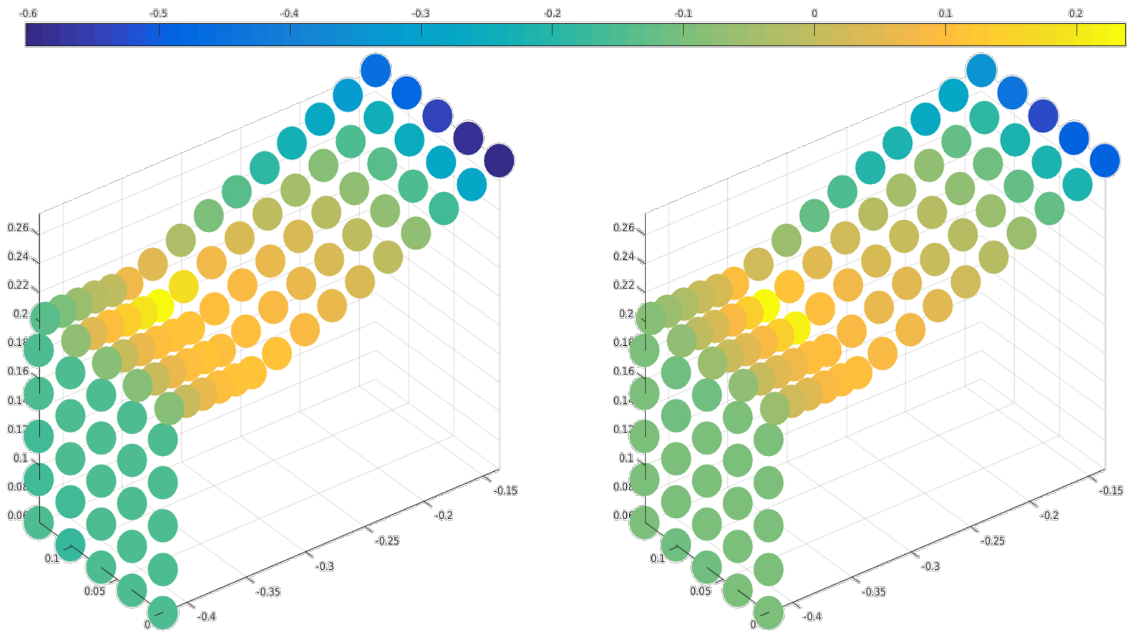

Figure 4.22: C_p plot for one half of the back of the body, left is wind tunnel data and right is the MINMOD simulation.

On the plot of overall pressure, figure 4.22, we can see that the pressure agrees very well except for on the base. There is also a difference where the C-pillar vortex interacts with the forward edge of the bootdeck which will be explained in detail later on.

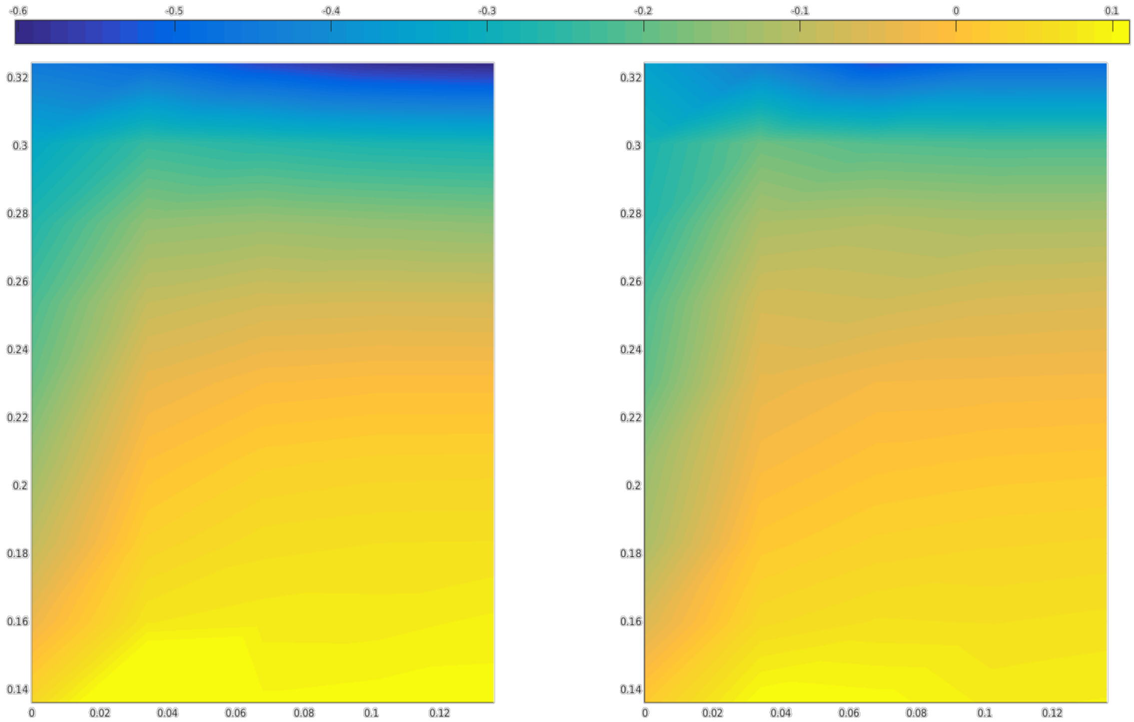

Figure 4.23: C_p plot for one half of the backlight, left is wind tunnel data and right is the MINMOD simulation.

The pressure on the backlight, figure 4.23, agrees very well from the simulation with that of the wind tunnel experiments. There is a slight difference at the top of the backlight where the pressure is higher in the simulation than it is in the experiment there is also a narrower area of high pressure in the simulation.

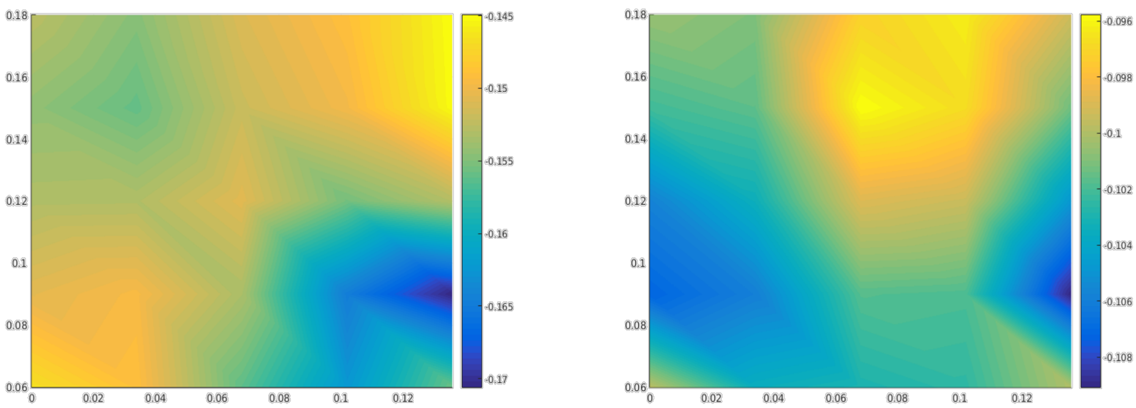

Figure 4.24: C_p plot for one half of the base, left is wind tunnel data and right is the MINMOD simulation.

The pressure on the base, as shown in figure 4.24, has a similar shape to that of the SMART simulation and does not agree well with the experimental data. The average base pressure is also slightly lower than that of the experiments.

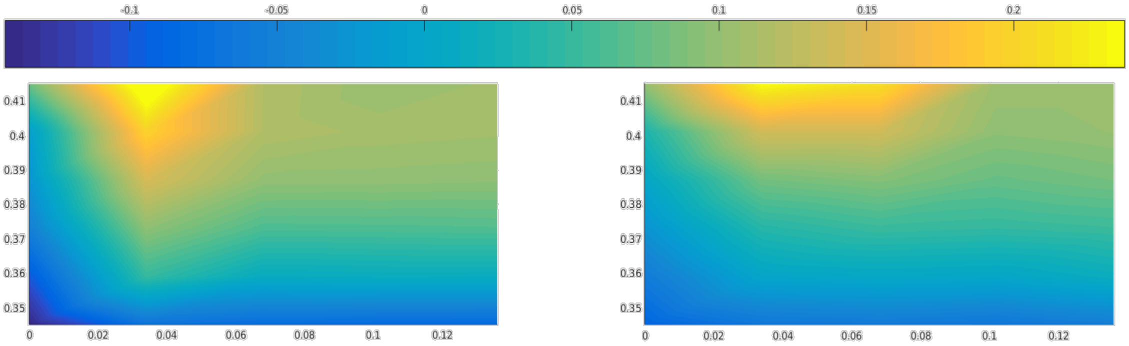

Figure 4.25: C_p plot for one half of the bootdeck, left is wind tunnel data and right is the MINMOD simulation.

The pressure on the bootdeck, figure 4.25, agrees fairly well with that of the experiment except for the area where the C-pillar vortex interacts with the bootdeck where the high pressure area is much wider and shorter than that of the experiment.

4.2 SMART simulation

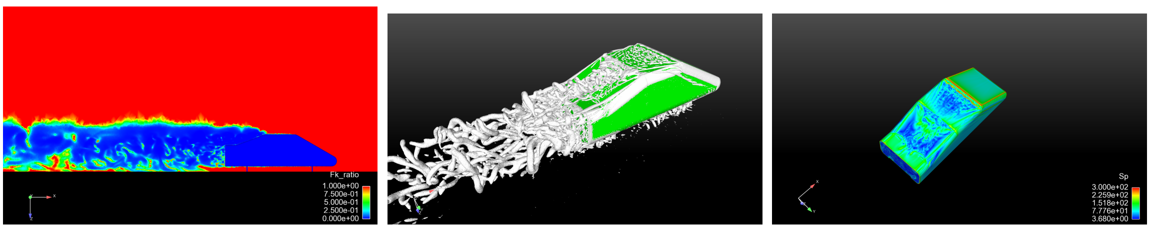

(a) F_k (b) CFL (c) Y^+

Figure 4.26: Figures displaying temporal and spatial resolution of the simultaion. The plane is a XZ plane at Y=0. All three are graded from 0 to 1.

In comparing these results to those of the MINMOD simulation we can see that a much higher amount of small scale flow structures are resolved and the average base pressure is much closer to that of the wind tunnel experiment. We can also see that the spanwise and streamswise wall resolution is similar to that of the MINMOD simulation but the f_k values are much lower overall. The drag values are also much closer than those of the experiment than the MINMOD simulation and are within roughly 0.75% which is a great result. However the lift values are still 126% higher than those from the experiment.

Flow field

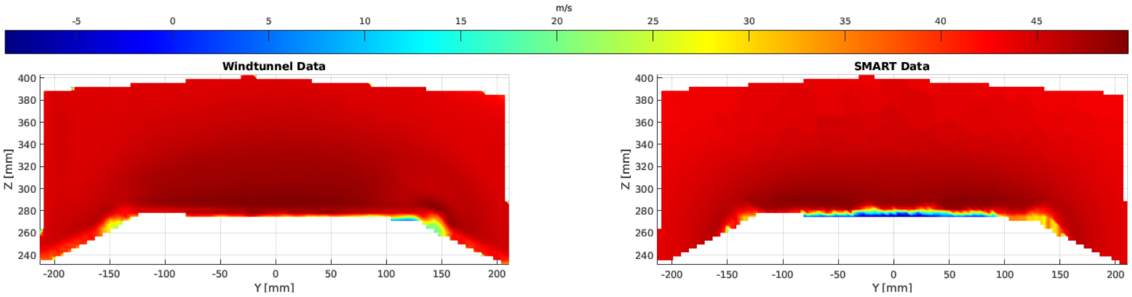

Figure 4.27: YZ plane at x=-140mm, showing flow magnitude in X direction.

Figure 4.27 shows that the flow over the C-pillars is fairly similar and the far field is very similar. It however shows a large difference close to the center line where the beginning of separation can be seen, since there is recirculation along the wall of the backlight.

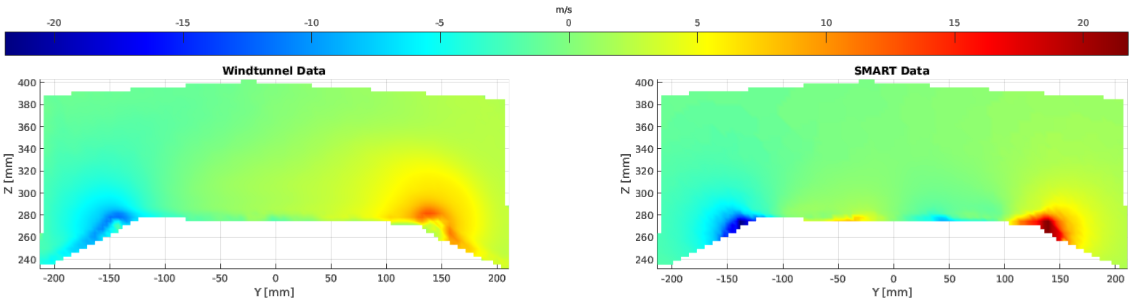

Figure 4.28: YZ plane at x=-140mm, showing flow magnitude in Y direction.

Figure 4.28 shows a similar flow field to that of the MINMOD simulation but in this case with a slight crossflow close to the center line along the backlight of the body. The C-pillar flow is well predicted but the gradient is too high which means that the areas of higher velocity are smaller in the simulation than they are in the experiment.

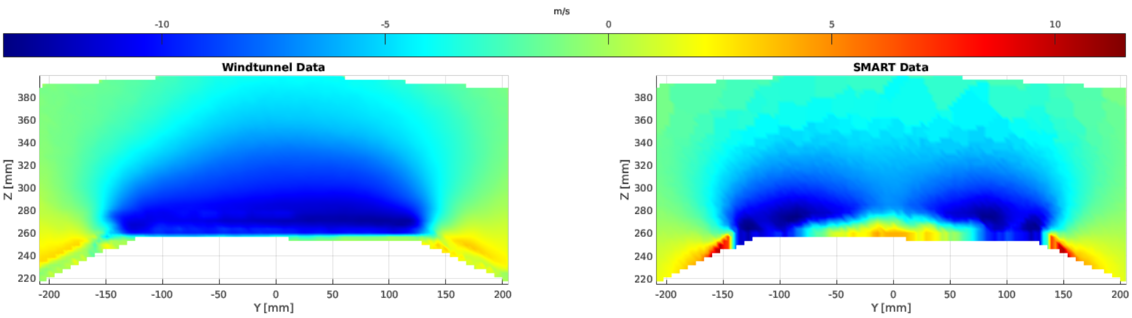

Figure 4.29: YZ plane at x=-190mm, showing flow magnitude in Z direction.

Figure 4.29 shows a lack of asymmetry in the simulation that is present in the experimental data and shows a developed separation in the simulation data as well as a much higher velocity along the C-pillars. The flow slightly further away from the C-pillars is well in agreement with the experimental data.

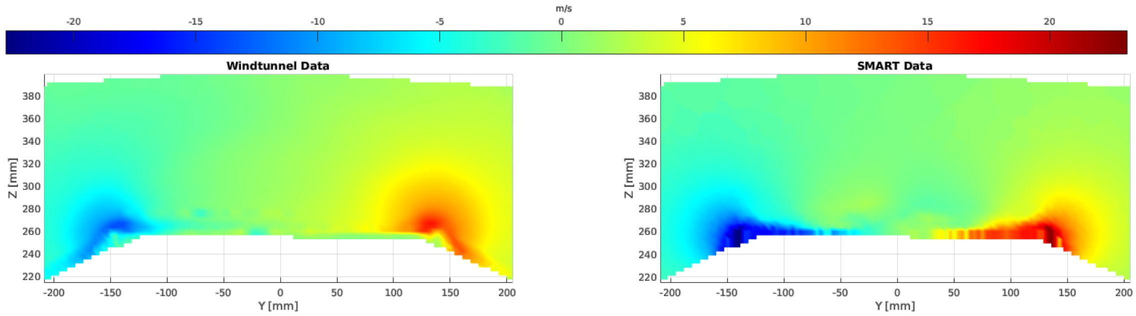

Figure 4.30: YZ plane at x=-190mm, showing flow magnitude in Y direction.

Figure 4.30 shows a slight asymmetry in both the simulation and the experimental data but it is reversed, where the high velocity area over the C-pillars is larger on one side than the other. In the experimental data the Y=140 area is larger with the Y=-140 area slightly larger in the simulation data. This is also true for the flow field further away from the high velocity area with a fairly similar gradient in the two data sets, but slightly higher gradient for the simulation.

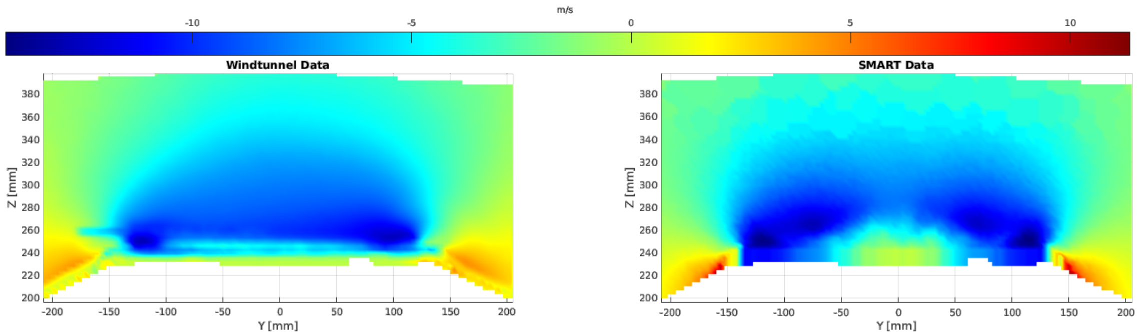

Figure 4.31: YZ plane at x=-240mm, showing flow magnitude in Z direction.

Figure 4.31 further shows the difference in separation where the simulation shows a completely separated flow and the experiment shows the beginning of separation and the asymmetry of the bulk flow in the Z direction. The bulk of the downwards flow over the backlight is also wider for the simulation than it is for the experiment.

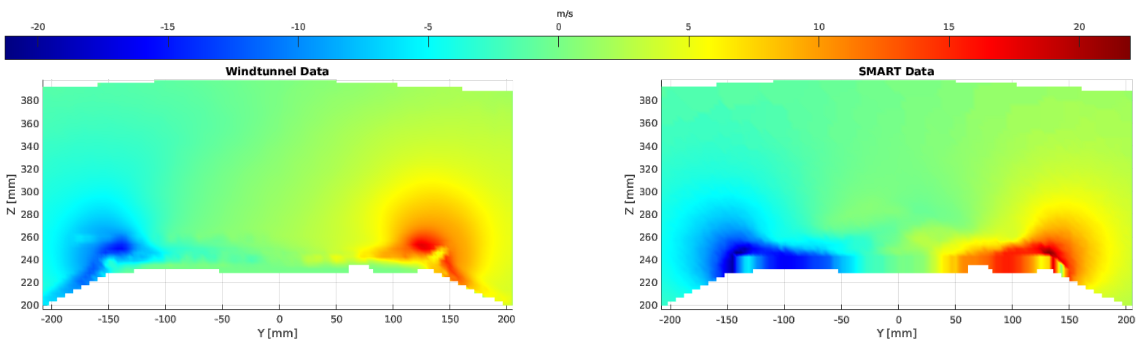

Figure 4.32: YZ plane at x=-240mm, showing flow magnitude in Y direction.

Figure 4.32 shows the continued slight asymmetry for the Y direction of the flow as was previously shown. At this plane there is a significantly larger amount of crossflow in the simulation than there is in the data from the experiments. The accelerated flow over the C-pillars is also wider outwards in the experimental data than it is in the simulation for this plane.

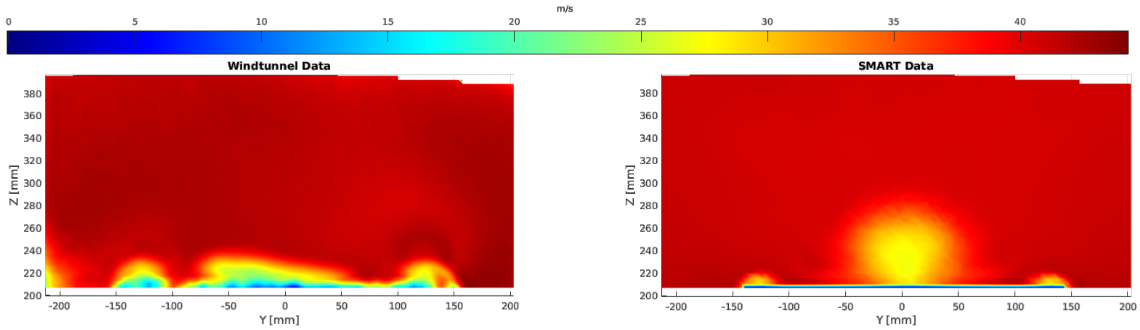

Figure 4.33: YZ plane at x=-420mm, showing flow magnitude in X direction.

In figure 4.33 it can be seen that the area of separation has affected the flow downstream at the edge of the body. Here it is asymmetric on the center line in the experimental data and the vortex area is much smaller in the simulation than it is in the experimental data.

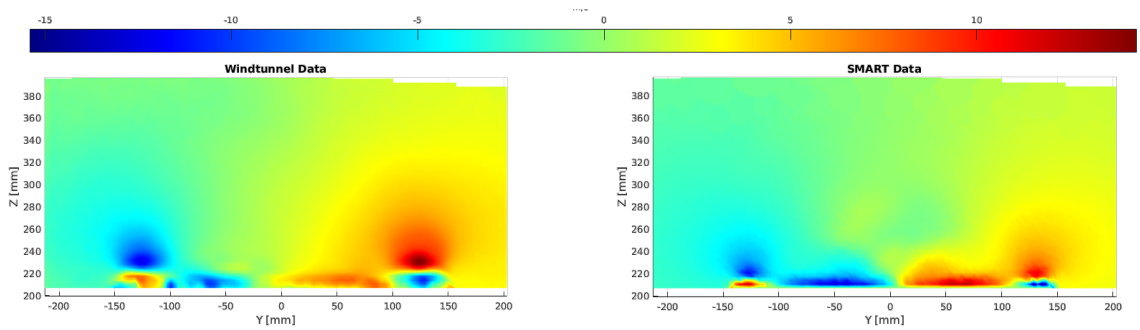

Figure 4.34: YZ plane at x=-420mm, showing flow magnitude in Y direction.

Figure 4.34 shows an asymmetry for both data sets but as was seen in figure 4.32 and 4.30 it is switched to the other side. The vortex location is closer to the body as well as weaker and smaller in the simulation than it it in the experiment. The crossflow of the simulation is however much stronger than that of the experiment and contains a slight assymmetry.

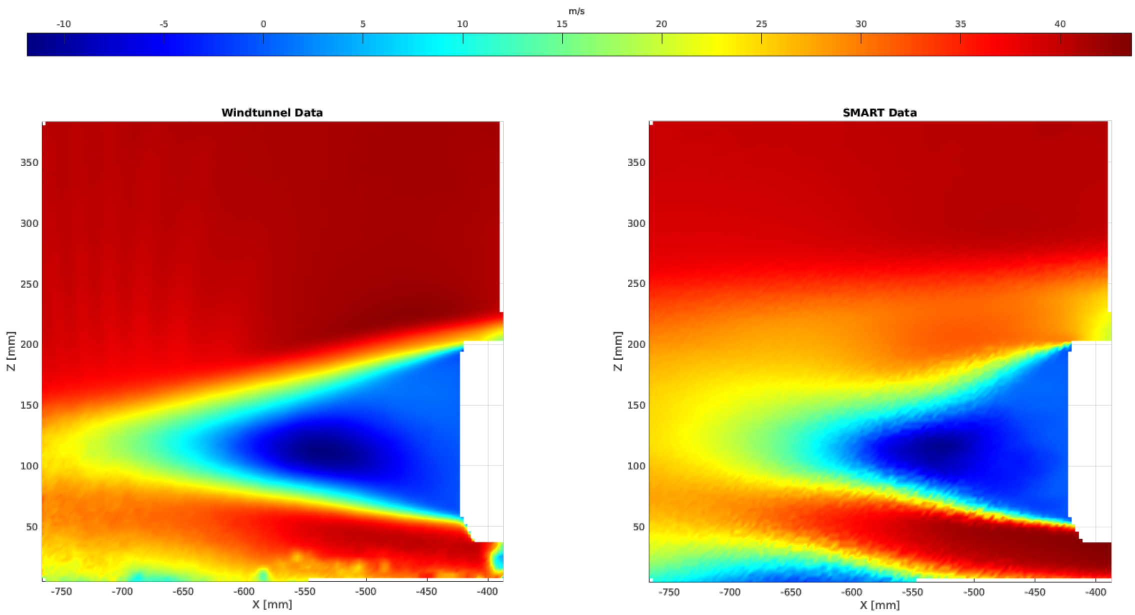

Figure 4.35: XZ plane at Y center line, showing flow magnitude in X direction.

Figure 4.35 shows a similar closure length of the base wake but with a significantly different shape of the top of the wake compared to the experimental data. The bottom of the base wake agrees well with the experimental results. The far field is greatly affected from the earlier separation on the backlight where the velocity above the bootdeck is much lower than that of the experimental data.

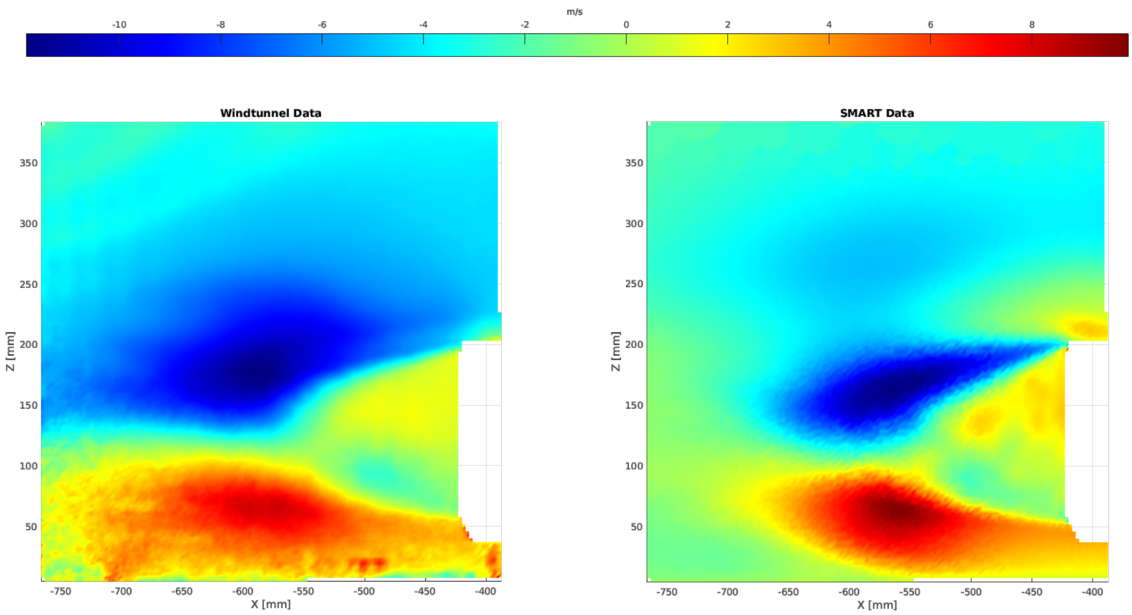

Figure 4.36: XZ plane at Y center line, showing flow magnitude in Z direction.

Figure 4.36 shows good agreement between the simulation and experiment for the base wake until x=-650 where it diverges from the experimental values. Behind this the flow is poorly predicted and above the bootdeck the flow is also poorly predicted.

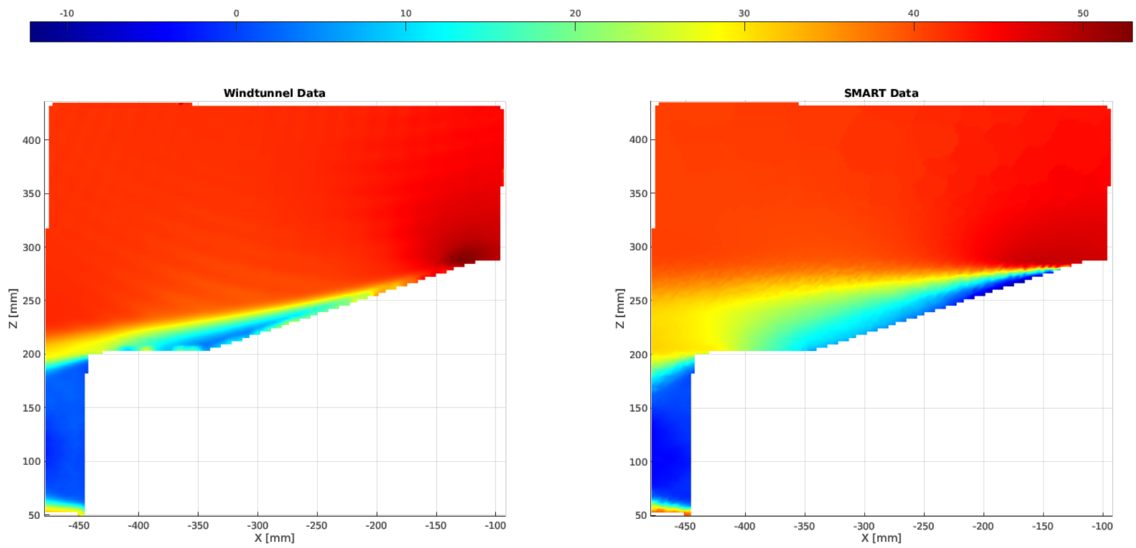

Figure 4.37: XZ plane at Y center line, showing flow magnitude in X direction.

Figure 4.37 shows how the early separation affects the backlight flow. The backlight recirculation is much smaller and located very far up along the backlight in the simulation. In the experimental data the recirculation is located at the very end of the backlight.The acceleration over the top curvature between the roof and backlight which indicates that the separation occurs at the curvature on the top of the roof.

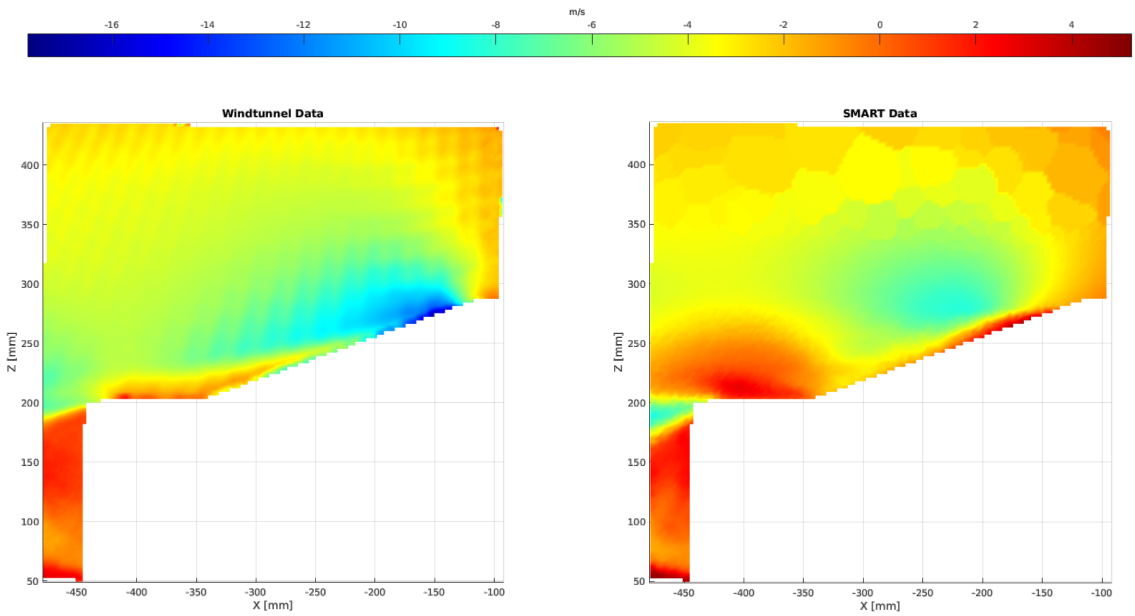

Figure 4.38: XZ plane at Y center line, showing flow magnitude in Z direction.

Figure 4.38 shows very poor agreement between simulation and experiment along the center line of the backlight with very early separation resulting in poor results along the center line. The bottom half of the base wake still is in good agreement but the top half of the base wake is in very poor agreement.

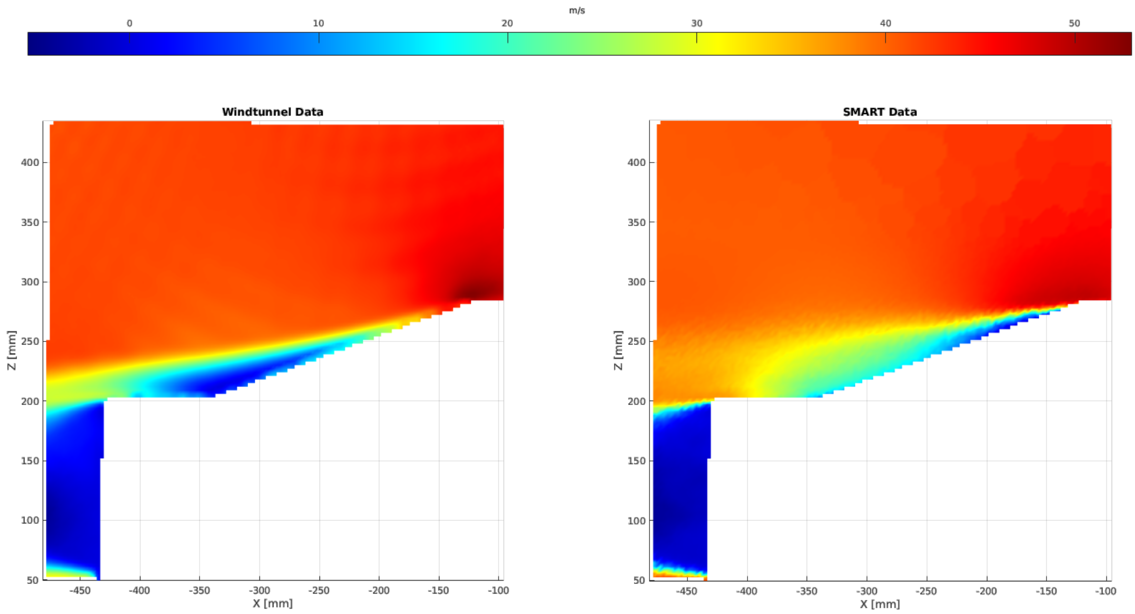

Figure 4.39: XZ plane at Y=-45mm, showing flow magnitude in X direction.

Figure 4.39 shows a similar difference between simulation and experiment as Figure 4.37 but with the separation bubble closing earlier than on the center line. The separated flow in the simulation is very different compared to that of the experiment where it does not close from the top towards the bootdeck but rather from the sides as can be seen in figure 4.32 and 4.34.

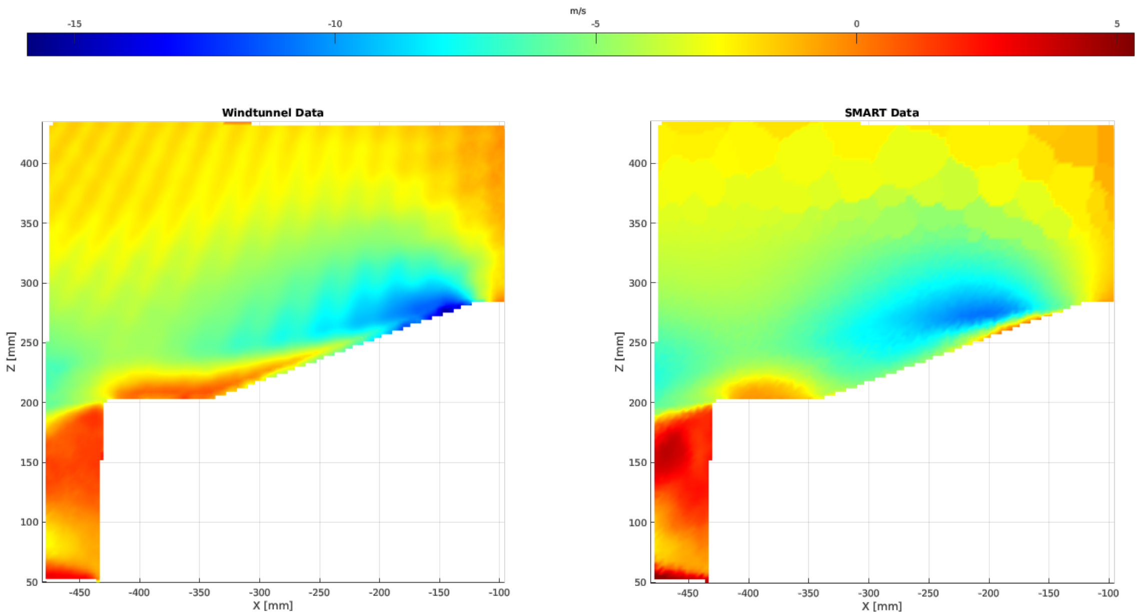

Figure 4.40: XZ plane at Y=-45mm, showing flow magnitude in Z direction.

Figure 4.40 shows the early separation of the flow over the roof edge to turn downwards and aligns the flow towards that of the experimental data as seen round x=-200 in figure 4.39. It also shows that the separation along the roofline does not have a strong recirculation, which it does in the experimental data. The base wake is much better predicted than it is along the center line of the body as seen in figure 4.38.

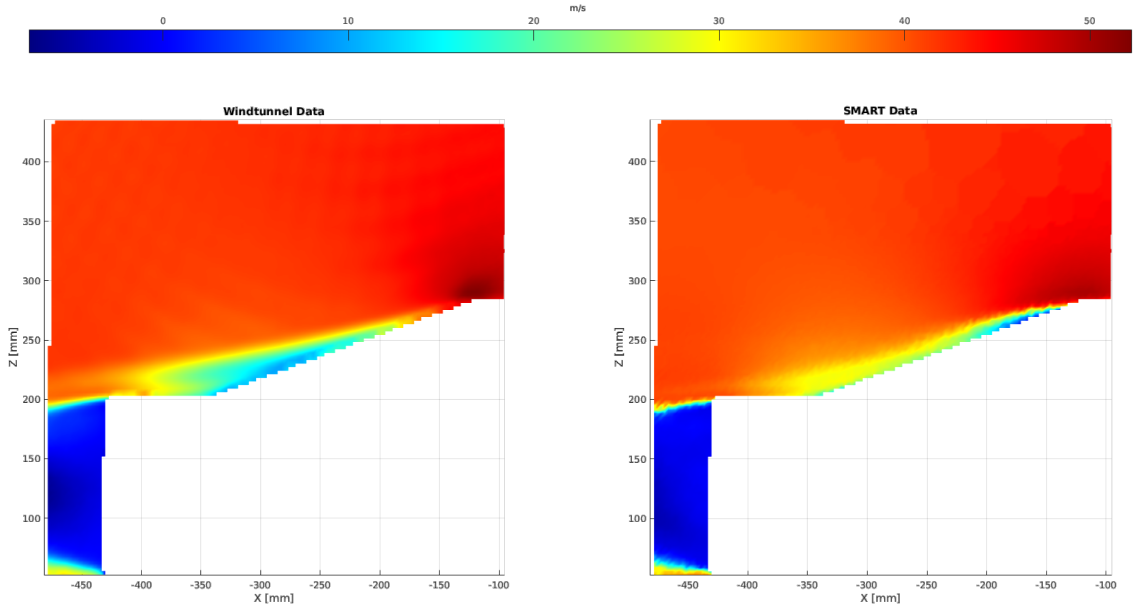

Figure 4.41: XZ plane at Y=-75mm, showing flow magnitude in X direction.

Figure 4.41 shows the same erroneous point of separation but with a fairly decent prediction of the bulk flow. The acceleration over the roof edge is also better predicted in this plane however it is still under predicted with separation most likely occurring at the radius of the roof to backlight. The base wake at this plane also looks well predicted with top and bottom angles as well as the internal flow being well predicted.

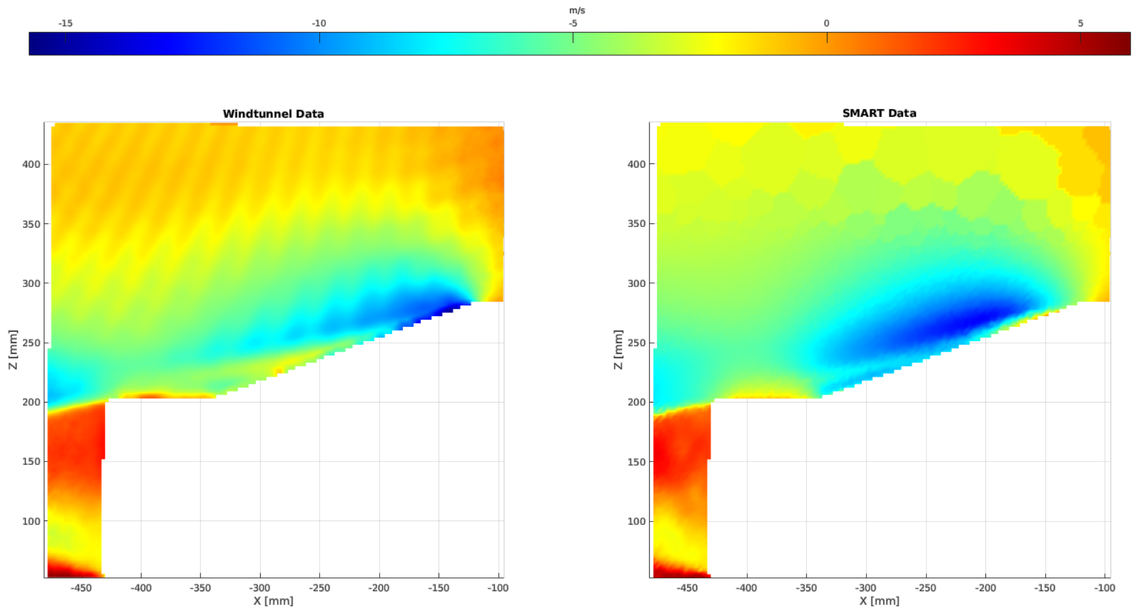

Figure 4.42: XZ plane at Y=-75, showing flow magnitude in Z direction.

Figure 4.42 shows good agreement between the two data sets from x=-360 and rearwards but the flow over the backlight has the same erroneous separation as has been shown in other figures. There seems to be a reattachment of the flow further down the backlight in the simulation but with the experiment showing a fairly strong separation at x=-200.

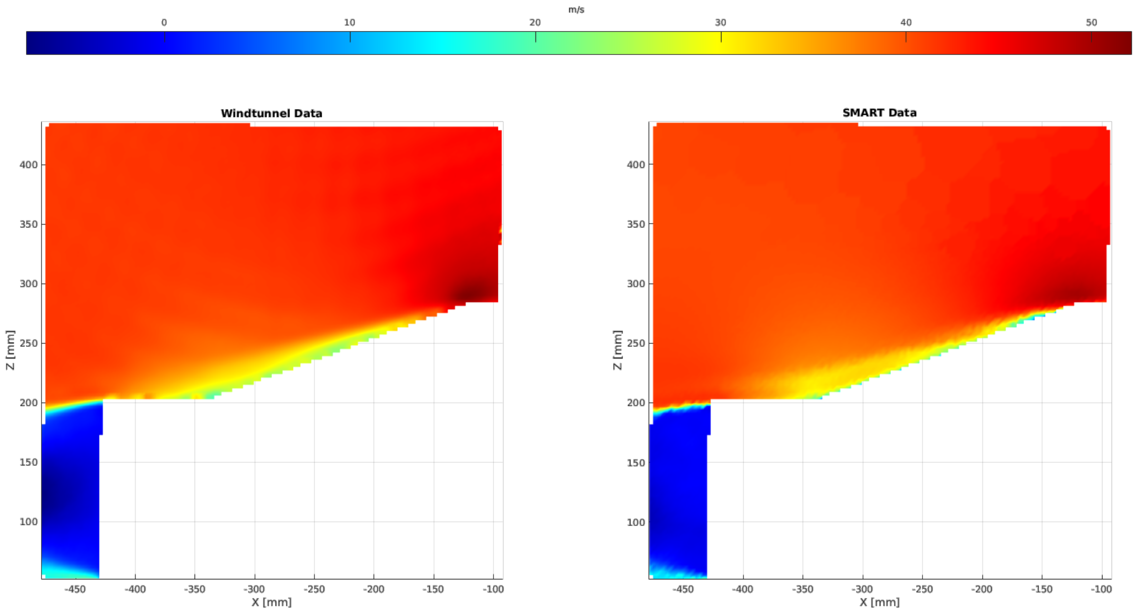

Figure 4.43: XZ plane at Y=-90mm, showing flow magnitude in X direction.

Figure 4.43 shows many similarities between the simulation and experimental data with the base wake being very well predicted and the flow over the upper backlight also being well predicted. The flow over the bootdeck however differs significantly between the simulation and experiment with the separation of the simulation not reattaching to the bootdeck which it does for the experimental data.

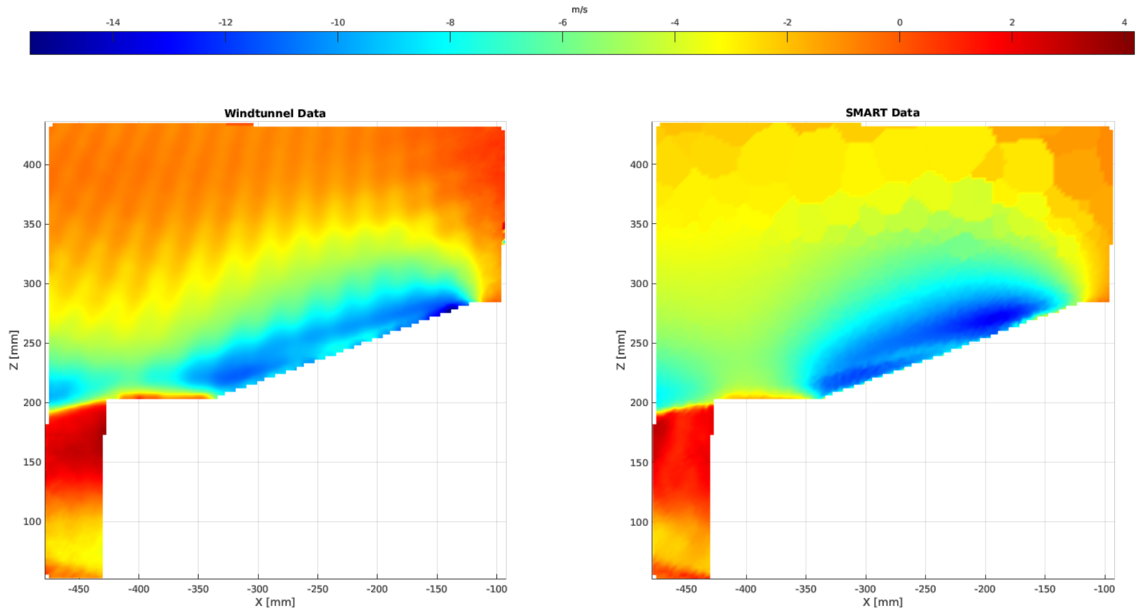

Figure 4.44: XZ plane at Y=-90, showing flow magnitude in Z direction.

Figure 4.44 shows the same good agreement of flow behind x=-400 in the Z directional flow. The flow along the backlight is similar to that of the experimental data with most of the features present in the experimental data are also present in the simulation such as the central streak of slower flow. There is however a larger area of high magnitude velocity over the backlight in the simulation. In the connection between the backlight and bootdeck there is a difference where the downwards flow continues further rearwards in the experimental data than it does in the simulation which would indicate as seen in figure 4.43 that the flow does not reattach again. This could also be explained by the crossflow seen in figure 4.34 to show where the flow comes from instead of reattaching.

Pressure data

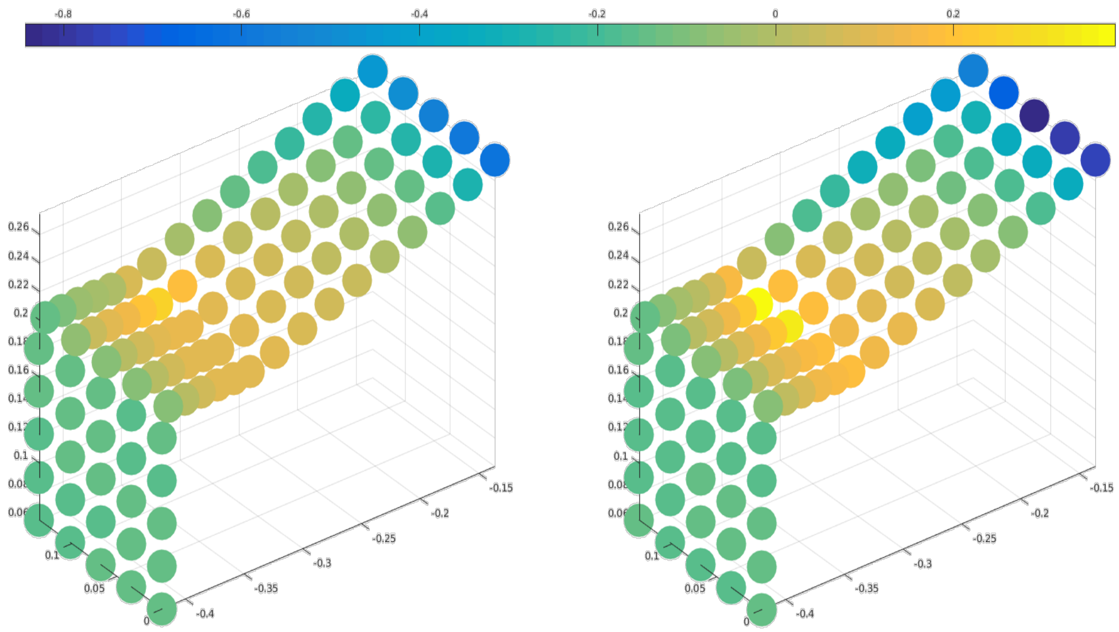

Figure 4.45: C_p plot for one half of the back of the body, left is wind tunnel data and right is the SMART simulation.

As can be seen in figure 4.45 the pressure on the base of the model is very well predicted in this simulation but the backlight and front of the bootdeck is not as well predicted with the top center and edge of the backlight being the poorest predicted with regards to pressure.

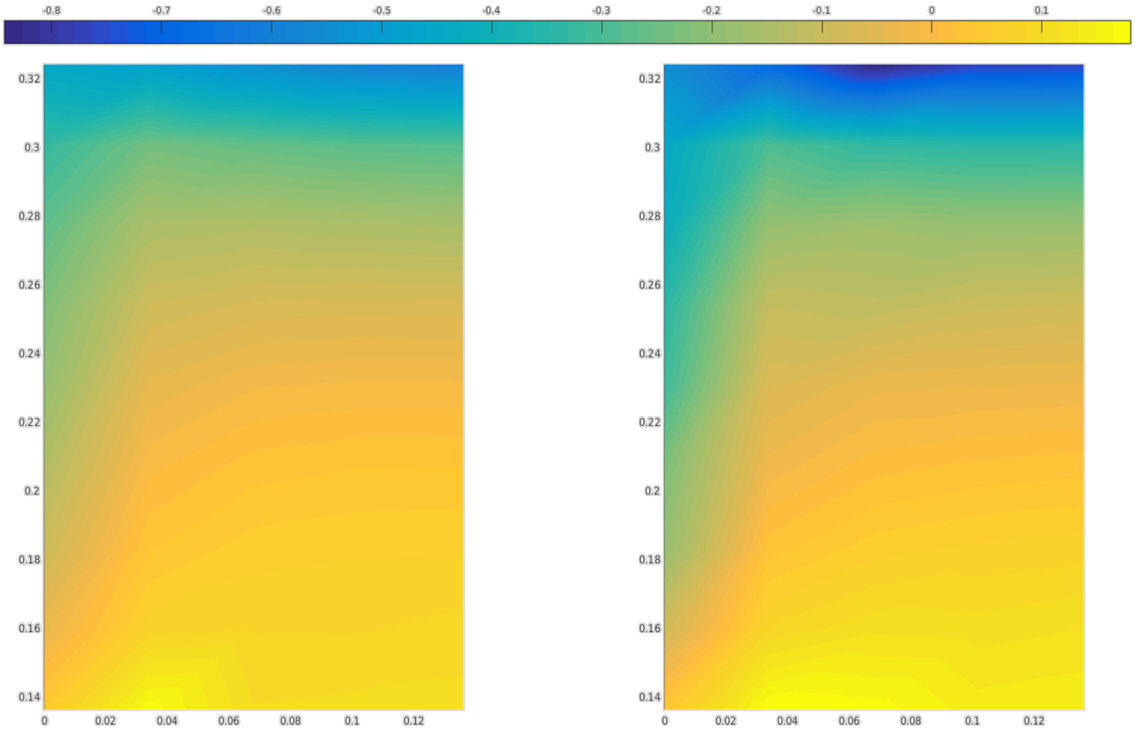

Figure 4.46: C_p plot for one half of the backlight, left is wind tunnel data and right is the SMART simulation.

Figure 4.46 shows that the general shape of pressure contrours are fairly similar on the backlight. The top of the backlight is the worst predicted pressure area where there is a larger pressure gradient along the backlight in the simulation than there is in the experiment.

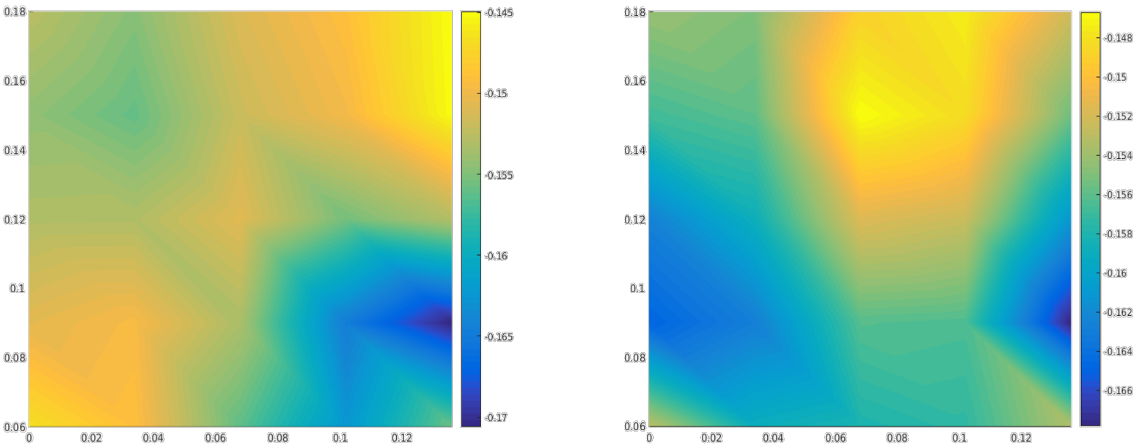

Figure 4.47: C_p plot for one half of the base, left is wind tunnel data and right is the SMART simulation.

As can be seen in figure 4.47 the pressure contours on the base are not well predicted with respect to location but the average pressure on the base is very close to that of the wind tunnel test.

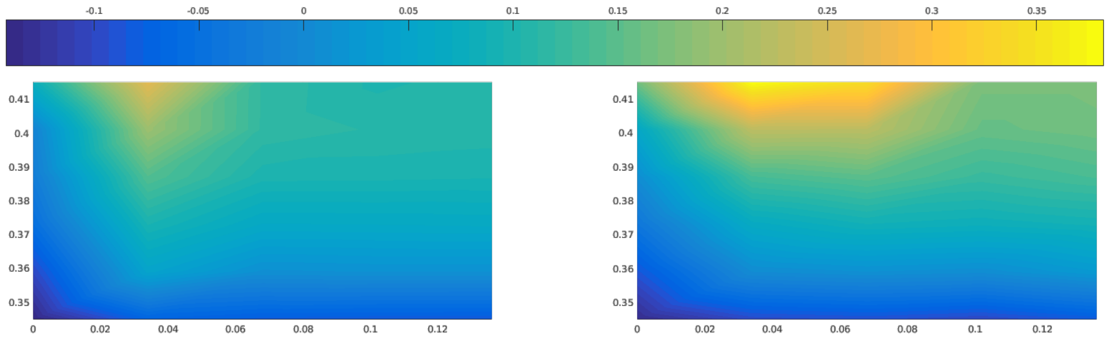

Figure 4.48: C_p plot for one half of the bootdeck, left is wind tunnel data and right is the SMART simulation.

On the bootdeck, as shown in figure 4.48, we can see that the pressure is far too high on the front half of the bootdeck. There is a much wider area of high pressure where the C pillar vortex interacts with the bootdeck and the experimental data shows a much narrower area of high pressure. The central forward region of the bootdeck also shows a too high pressure compared to the wind tunnel experiments.

5 Discussion

5.1 MINMOD

The differences in separation points is to be expected since that is something that is extremely hard to predict. The consequences of separation at the wrong point will in this case affect the downstream flow structures greatly as can be seen in the velocity plots. Explaining the difference in drag between the wind tunnel data and the data from the simulation could be done by pointing to the large difference in the base pressure. One should also consider the base wake difference and later separation causing a higher pressure along the backlight, both of which will reduce the drag. This could be used to explain the lower drag
Trying to figure out where the large error in lift comes from is significantly harder since the small differences in pressure along the backlight, bootdeck and center line of the body cannot explain the lift that is almost three times higher than that of the wind tunnel. This leads to the suspicion that the under body flow is not well predicted in the MINMOD simulation. This can partly be seen in the base wake plot in both the X and Z direction along the center line where the flow does not turn upwards as much as it does in the wind tunnel plots. Comparing the two simulations one can see how sensitive the flow over the backlight is with only a change in the discretization causing a completely different flow with much more crossflow and early separation. It does seem that even though there is separation present in the MINMOD simulation it appears too late and does not create the same separation bubble and recirculation that is present in the wind tunnel.
This along with the recirculation of the SMART simulation being significantly different from that of the wind tunnel even if early separation occurs indicates a difficulty of handling separated flows. The weak and small vortices at the end of the vehicle might indicate a too high rate of dissipation since the difference is much smaller further upstream. In comparison with other work done in [5] and [6] these results seem of insufficient accuracy and might be hampered the very sensitive nature of the flow over this specific body. The fact that the MINMOD discretization is as diffusive as it is compared to smart and CD might influence the separation to be delayed due to the diffusion of momentum through the boundary layer being over predicted.

5.2 SMART

The smart simulation shows significantly better drag and lift values which is to be expected with respect to the drag but not with lift when compared to the MINMOD simulation since the center line Cp plot shows much better prediction by the MINMOD simulation. There is a lot more small structures that are resolved in the SMART simulation as well, these might not be physical however and be numerically induced vortices. The resolution for the simulations are likely however of sufficient resolution to not produce numerical errors, the use of a central differencing scheme might have been useful however in this case. The bottom of the base wake is much more in line with the experimental values which might indicate a better predicted under body flow and thus explain the better predicted lift. The Smart simulation also shows a slight asymmetry even though it is not as strong as the one in the experimental data. The early separation most likely produces most if not all of the differences further downstream since it also creates a lower pressure along the backlight than there is in the wind tunnel or MINMOD simulation creating a stronger crossflow. The crossflow likely causes the problem of the airflow not reattaching on the backlight at sections a bit further out in the Y-direction on the bootdeck. This problem then further creates the much taller wake and different structures in the wake. The flow does seem to only heavily recirculate for a small area just beneath the roof line at the backlight and not fully separate like the flow does in the wind tunnel. The large discrepancy in the lift could also stem from an incorrectly calculated coefficient of lift from the wind tunnel data or in the simulations. This large of a difference in lift does not seem feasible considering the pressure measurements that exist do not differ by very much.

6

Conclusion

The conclusion of this work is that the PANS simulation model has decent potential if used correctly. There are however as of now too many things that can heavily influence the results, for example changing the discretization alters the drag by 6% and the lift by 30%. This is something that has to be further investigated since such a small change influences the results from not separating along the backlight until the end of the backlight to it separating along the roof line. Drag values are very well predicted for the SAE body but lift is very poorly predicted compared to that of the wind tunnel which needs to be investigated. It is also evident that there are a lot more smaller structures developed in the SMART simulation, if these are physical or not is however not possible to say at this time.

Bibliography

[1] C. Hoever *The simulation of car and truck tyre vibrations, rolling resistance and rolling noise*. Chalmers University of Technology, 2014.

[2] B.P.Leonard *Simple High-AccuracyResolution Program for Convective Modelling of Discontinuities*. Int.J.Numer. Meth. Eng., vol. 8, pp. 1291-1318, 1988.

[3] *AVL Fire 2014 Manual*. https://www.avl.com/fire2 , 2016.

[4] S. Girimaji *Partially-Averaged Navier-Stokes Model for Turbulence: a Reynolds-Avergaged Navier-Stokes to Direct Numerical Simulation Bridging Method*. Journal of Applied Mechanics, 2006.

[5] B. Basara, S. Krajnovic, S. Girimaji et al. *Near-Wall Formulation of the Partially Averaged Navier Stokes Turbulence Model*. AIAA Journal, 2012.

[6] S. Krajnovic, G. Minelli *Partially-averaged Navier-Stokes simulation of the flow around simplified vehicle*. PROCEEDINGS OF THE INTERNATIONAL CONFERENCE ON NUMERICAL ANALYSIS AND APPLIED MATHEMATICS 2014 (ICNAAM-2014).

[7] Lars Davidson *Fluid mechanics, turbulent flow and turbulence modeling*. URL: `http://www.tfd.chalmers.se/~lada/postscript_files/solids-and-fluids_turbulent-flow_turbulence-modelling.pdf`, 2016.

[8] J.C.R. Hunt, A.A. Wray and P. Moin. *Eddies, Streams, and Convergence Zones in Turbulent Flows*. Center for Turbulence Rereomh Proceedings of the Summer Program, 1988.

[9] R. Courant, K. Friedrichs, H. Lewy. *Über die partiellen Differenzengleichungen der mathematischen Physik*. (German) [*On the Partial Difference Equations of Mathematical Physics*. IBM Journal of Research and Development, 1967.] Mathematische Annalen 100, 1928

[10] Wood, D., Passmore, M., and Perry, A. *Experimental Data for the Validation of Numerical Methods - SAE Reference Notchback Model*. SAE Int. J. Passeng. Cars - Mech. Syst. 7(1):2014, doi:10.4271/2014-01-0590.

[11] Versteeg, Henk Kaarle and Malalasekera, Weeratunge. *An introduction to computational fluid dynamics: the finite volume method*. Pearson Education, 2007.

[12] Ami Harten. *High Resolution Schemes for Hyperbolic Conservation Laws*. Journal of Computational Physics 135, 260–278, 1997.

[13] P. H. Gaskell, A. K. C. Lau. *Curvature-compensated convective transport: SMART, A new boundedness- preserving transport algorithm*. International Journal for Numerical Methods in Fluids, 1988.

[14] Krajnović, S. and Minelli, G. *Partially-averaged Navier-Stokes simulation of the flow around simplified vehicle*. Proceedings of the International Conference on Numerical Analysis ans Applied Mathematics 2014.

[15] Darwish, M. S. *A new high–resolution scheme based on the normalized variable formulation*. Numerical Heat Transfer, Part B: Fundamentals, Volume: 24 Issue: 3 Page: 353-371, 1993.